Ore Geology Reviews 88 (2017) 23–42

Contents lists available at ScienceDirect

Ore Geology Reviews

journal homepage: www.elsevier.com/locate/oregeo

Geochemistry and chemical dating of uraninite in the Samarkiya area, central Rajasthan, northwestern India – Implication for geochemical and temporal evolution of uranium mineralization

Manoj Kumar Ozha [a], Dipak Chandra Pal [b], Biswajit Mishra [a,*], T. Desapati [c], T.S. Shaji [d]

[a] Department of Geology and Geophysics, Indian Institute of Technology, Kharagpur, 721302, India
[b] Department of Geological Sciences, Jadavpur University, Kolkata 700032, India
[c] Atomic Minerals Directorate for Exploration and Research, Visakhapatnam 530007, India
[d] Atomic Minerals Directorate for Exploration and Research, Thiruvananthapuram 695012, India

ARTICLE INFO

Article history:
Received 25 August 2016
Received in revised form 9 April 2017
Accepted 12 April 2017
Available online 13 April 2017

Keywords:
Aravalli-Delhi Fold Belt
Uraninite
Geochemistry
Chemical dating
Uranium mineralization

ABSTRACT

In the Samarkiya area, located at the central part of the Aravalli-Delhi Fold Belt (ADFB), uranium mineralization is hosted both by the basement Mangalwar Complex and the overlying supracrustal rocks of the Pur-Banera belt. The present study aims to appraise the geochemical and temporal evolution of uranium mineralization from the basement and the adjoining supracrustals in the Samarkiya area integrating textural features, geochemistry, and in situ U-Th-Pb_{Total} dating of uraninite.

Uraninite occurs as inclusions in the major rock forming minerals, viz. plagioclase, quartz, biotite, and chlorite. Based on the shape, location in the host mineral (well inside/at the grain boundary/along or connected to micro-cracks etc.) and association with other secondary uranium minerals, uraninites are classified into different groups, which are compositionally distinct, barring some exceptions. Integrating texture, geochemistry and in situ electron probe dating we propose that in addition to an old event at ~1.88 Ga in the basement rocks, there are two major events of uraninite formation at ~1.24–1.20 Ga and ~1.01–0.96 Ga in both the basement and supracrustal rocks. Although none of the pristine, unaltered uraninites that formed during the above mentioned events contain significant intrinsic minor or rare earth elements, the basement uraninites are consistently much enriched in thorium compared to those from the supracrustal. Based on the compositions, we propose that the basement uraninites formed from a high temperature magmatic/metamorphic fluid, whereas those in the supracrustal rocks crystallized from a low temperature, presumably oxidized fluid. Back-scattered electron images, X-ray elemental mapping of selected elements and EPMA spot analysis of large uraninite grains (both from the basement and the supracrustals) collectively demonstrate that subsequent to the major mineralizing event at ~1.24–1.20 Ga, the mineralized rocks were subjected to fluid-mediated alteration, which resulted in ∑REE + Y- and Si (Ca)-enrichment of existing ~1.24–1.20 Ga uraninites in the basement and supracrustal rocks, respectively. We cannot constrain the exact timing of this alteration event. However, as this event altered the ~1.24–1.20 Ga uraninites and as spot ages of the altered grains yield ages largely between ~1.24 and 0.96 Ga, it is reasonable to place this event between the second and third stages of uranium mineralization/mobilization at ~1.20 Ga and ~1.01 Ga, respectively. The last event that took place at ~1.01–0.96 Ga most likely represent an episode of recrystallization/alteration of existing uraninite leading to complete Pb-loss and resetting of the isotopic clock. However, we do not entirely reject the possibility of neo-mineralization.

The discrete events deciphered from uraninite in the Samarkiya area can also be broadly linked to some major magmatic-metamorphic events, identified from other independent studies, in the ADFB. For example, the earliest ~1.88 Ga event displayed by basement uraninite is most likely related to a pervasive magmatic-metamorphic event (~1.86–1.82 Ga) that affected the basement, whereas the last/latest event ~1.01–0.96 Ga can be linked to a pervasive metamorphic event that affected perhaps the entire ADFB. This last episode can also be linked to the tectono-thermal event related to the Rodinian amalgamation.

* Corresponding author.
E-mail address: bmgg@iitkgp.ac.in (B. Mishra).

http://dx.doi.org/10.1016/j.oregeorev.2017.04.010

The ~1.24–1.20 Ga event appears to be somewhat enigmatic in the context of well-known geological events in the area. However, based on some very recently published data, we interpret this to be a post-peak metamorphic (~1.37–1.35 Ga) hydrothermal event or even a new metamorphic event, hitherto unknown.

1. Introduction

The Proterozoic unconformity-related uranium deposits (e.g., Athabasca Basin, Canada; Kyser et al., 2000) constitute the third largest reasonably assured uranium resources of the world (IAEA, 2016). These very high grade (e.g., ~20% U_3O_8 at McArther deposit; Jefferson et al., 2007; Mercadier et al., 2013) large tonnage deposits, particularly those of Canada, collectively top the lowest cost category of the reasonably assured resources (IAEA, 2016). Consequently, Proterozoic unconformities are extensively explored as potential environs for uranium mineralization. Such deposits presently constitute ~9.95% of India's reasonably assured resources (IAEA, 2016). Some of the deposits associated with the Proterozoic rocks in India include those located in the Cuddapah basin (Rao et al., 2010; Deb and Pal, 2015; and references therein) and in the Singhbhum Shear Zone (Pal and Rhede, 2013) (Fig. 1a). The ~700 km long NNE-SSW trending Aravalli-Delhi Fold Belt (ADFB, Fig. 1a and b), being the largest Proterozoic belt in the northwestern India, has attracted the interest of the Atomic Minerals Directorate for Exploration and Research (AMDER), an organization responsible for U exploration in India. Subsequently, significant radioactive anomalies were reported from the metasedimentary rocks of the ADFB during the last two decades (viz., Umra and Rohil deposits near Udaipur and Jaipur, respectively in Rajasthan; Fig. 1b). In addition, >200 potential sites of anomalous radioactivity have been identified in and around the ~320 km long zone of albitite-microcline-pyroxinite, also referred to as the "Albitite line" (Ray, 1990) (Fig. 1b), in Rajasthan and Haryana (Singh et al., 2013).

The central part of the ADFB hosts the polymetamorphic terrain of the Banded Gneissic Complex (BGC; Gupta, 1934; Heron, 1953; Fig. 1b), which forms the basement to the supracrustal rocks of the Pur-Banera basin (PB; Fig. 1b), where the present investigation is carried out. In 2005, the AMDER discovered surface radioactive anomaly from the Samarkiya area, within the PB (Fig. 1c) and thereby considered the area as a potential target for uranium exploration. Subsequent petrographic and X-ray diffraction (XRD) studies revealed U-enriched minerals from the basal Pur quartzite of the Samarkiya area (Shaji et al., 2007). Shaji et al. (2007) proposed episodic uranium mineralization, involving mobilization, during the protracted magmatic/metamorphic evolution (~1.9–1.4 Ga) of the host rocks. However, detailed geochemical characters and temporal status of individual uranium mineralization/mobilization events, linked to tectono-metamorphic evolution of the host rocks, have so far eluded us.

In the Samarkiya area, uraninite is volumetrically the most abundant U-bearing mineral (Shaji et al., 2007). Amongst all the primary U-bearing minerals, uraninite hosts the highest U-content in its structure (i.e., up to 88.2 wt%). Due to auto-oxidation caused by radioactive decay of uranium, pure uraninite ($U^{+4}O_2$) phase is very rare in nature (Dahlkamp, 1993), and thereby the non-stoichiometry and defects in the mineral favors cationic substitution (Janeczek and Ewing, 1992), which modifies and alters its formula to $(U^{4+}_{1-x-y-z}U^{6+}_{x}REE^{3+}_{y}M^{2+}_{z})\ O_{2+x-(0.5y)-z}$ (Janeczek and Ewing, 1992; Finch and Murakami, 1999). Previous studies have demonstrated that uraninite is chemically active and readily exchanges elements or recrystallizes during subsequent fluid circulation events (Grandstaff, 1976; Kotzer and Kyser, 1993). Additionally, the content of trace (REEs and Y; hereafter ∑REY) and minor (Si, Ca, Fe, Al, K, and Na) elements within uraninite is a function of the physico-chemical conditions (temperature, redox state, and fluid composition) prevalent during uraninite formation (Alexandre and Kyser, 2005; Bonhoure, 2007; Mercadier et al., 2011; Eglinger et al., 2013; Pal and Rhede, 2013). Consequently, the concentrations of other elements in uraninite can act as geochemical tracers pertinent to its environment of formation. Further, geochemical characterization in conjunction with in situ dating of uraninite can provide constraints on the timing of mineralization and subsequent alteration, if any (Kempe, 2003; Deditius et al., 2007; Pal and Rhede, 2013). In this study, integrating geochemical characteristics and in situ chemical dating of uraninite, we aim at deciphering the mineralization types and geochemical vis-à-vis temporal evolution of uraninite.

2. Geological setting

2.1. Regional Geology

The ADFB comprises three major geological units, which in chronological order, from oldest to youngest, include the Banded Gneissic Complex (BGC), the Aravalli Supergroup and the Delhi Supergroup (Gupta, 1934; Heron, 1953; Raja Rao, 1976; Gupta et al., 1997; Fig. 1b). The BGC is divided into two disconnected terrains, BGC-I and BGC-II respectively constituting the southern and the central parts. The BGC-I is dominated by tonalite-trondhjemite-granodiorite suite and granitoids of the Archaean age (3.30–2.50 Ga; Wiedenbeck and Goswami, 1994; Roy and Kröner, 1996; Wiedenbeck et al., 1996). The BGC-II includes meta-igneous granulites (Sandmata Complex), and the meta-granitoids, amphibolites, and metasedimentary rocks, namely the Mangalwar Complex (MC; Guha and Bhattacharya, 1995). The rocks of the BGC-II mainly display Paleo-Neoproterozoic ages with vestiges of Archaean component (i.e., ~2.50–0.95 Ga) (Buick et al., 2006, 2010; Bhowmik et al., 2010; Roy et al., 2012; Ozha et al., 2016a). They are polychronous in nature, preserving Proterozoic crustal unit with an early metamorphic event (5.5 kbar and 520–550 °C) at ~1.82 Ga and a later high pressure event (8.0 kbar and 590–640 °C) at ~0.95–1.05 Ga (Buick et al., 2006, 2010; Bhowmik et al., 2010; Ozha et al., 2016a).

The MC constitutes vast stretch of schist and para- to ortho gneisses in the western part (i.e., at the contact of Sandmata Complex) of the BGC-II (Buick et al., 2006). On the contrary, in the central parts, the MC host garnetiferous biotite schist, which is unconformably overlain by the linear supracrustal belt of PB that evolved as pull-apart basin (Sinha-Roy et al., 1998) starting at ~1.74 Ga (Ozha et al., 2016a). The PB is a major syncline comprising rock units of quartzite/conglomerate (Pur Formation), metapelites, amphibolites, calc-silicate gneisses (Rewara Formation), banded iron formations (Tiranga Formation), and quartzite, mica schist with intercalations of marble and calc-silicate bands (Samodi Formation) (Fig. 1c). According to the recent petrological and geochronological studies of Ozha et al. (2016a), both the basement (MC) and the supracrustal (PB) rocks were subjected to two discrete amphibolite facies metamorphic events at ~1.37–1.35 Ga and ~1.05–0.99 Ga. In addition, a much older Paleoproterozoic

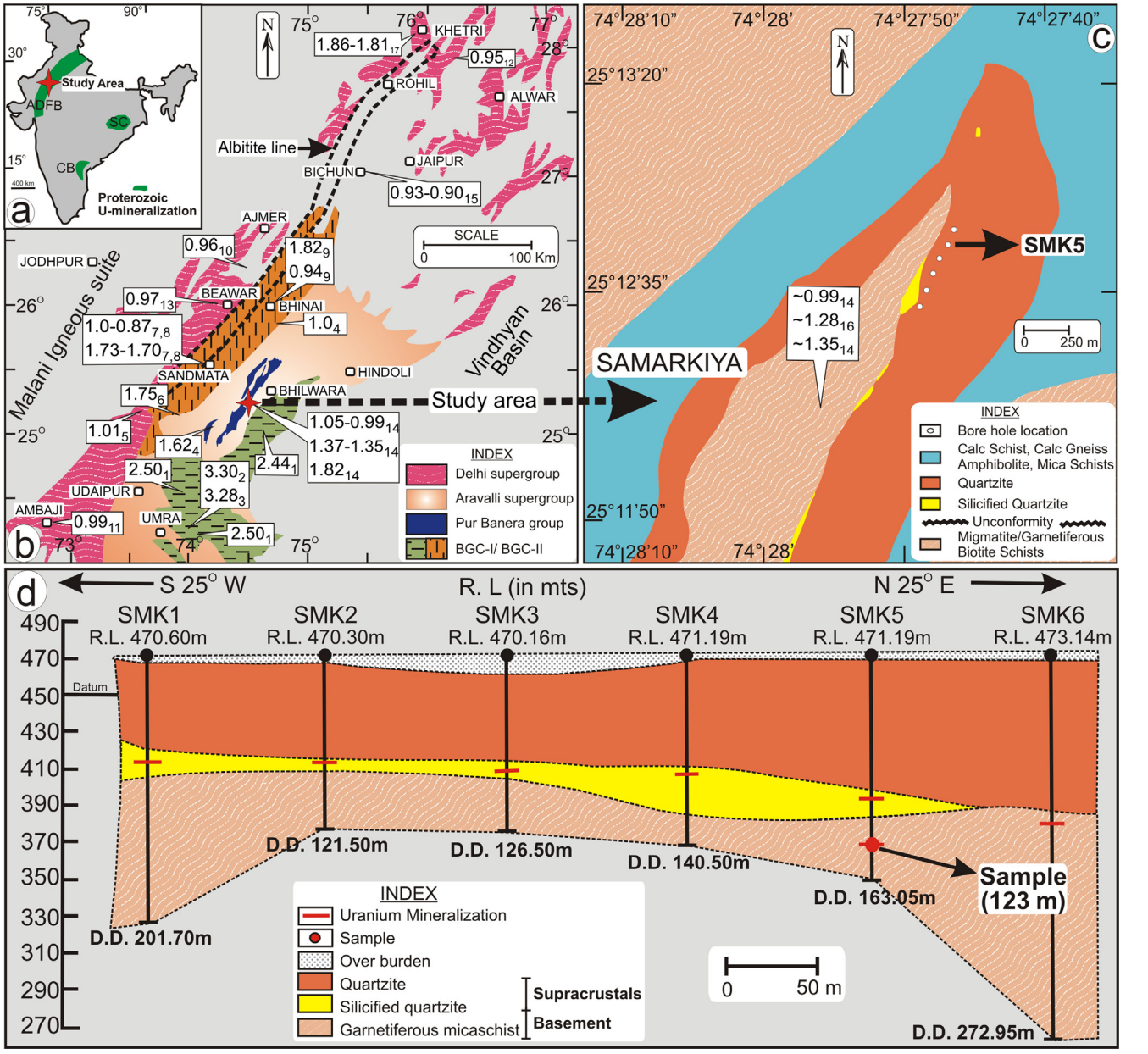

Fig. 1. (a) A map of India showing locations of Proterozoic uranium mineralization and the Aravalli-Delhi Fold Belt (ADFB); (b) Regional geological map of the ADFB, showing the distribution of different lithological components (modified after Heron, 1953; Gupta et al., 1997; Ozha et al., 2016a); chronology of the major geological events are after (1) Wiedenbeck et al. (1996); (2) Gopalan et al. (1990); (3) Wiedenbeck and Goswami (1994); (4) Hazarika et al. (2013); (5) Volpe and Macdaugall (1990); (6) Biju-Sekhar et al. (2003); (7) Bhowmik et al. (2010); (8) Sarkar et al. (1989); (9) Buick et al. (2006), (2010); (10) Tobisch et al. (1994); (11) Deb et al. (2001); (12) Pant et al. (2008); (13) Pandit et al. (2003); (14) Ozha et al. (2016a); (15) Yadav et al. (2016); (16) Hazarika et al. (in press); (17) Kaur et al. (2017); the black dashed line marks the limits of Albitite line (after Ray et al., 1990; Singh et al., 2013); all the ages shown (in Ga) are lithology specific rather than their locations; (c) Geological map of the Samarkiya area (modified after the Atomic Minerals Directorate for Exploration and Research, AMDER), showing the location of the six bore holes; (d) Longitudinal section (modified after the AMDER) along the six bores holes (shown in 'c') showing the distribution of different litho units and sample location. CB: Cuddapah Basin, SC: Singhbhum Craton.

metamorphic event (~1.82 Ga) (Buick et al., 2010; Ozha et al., 2016a) has been recorded from the basement MC. Furthermore, recently, Hazarika et al. (in press) reported a hydrothermal event in the MC rocks at ~1.28–1.27 Ga postdating the ~1.37–1.35 Ga peak metamorphism. Although, the BGC terrain has experienced several events of granitic magmatism in late Archaean-early Proterozoic (~3.00–2.40 Ga; Choudhary et al., 1984; Gopalan et al., 1990; Roy and Kröner, 1996; Wiedenbeck et al., 1996) elsewhere (viz., Berach granite, Gingla granite, Untala granite, Amet granite, Jahazpur granite, and Udaisagar granite), such felsic magmatism has not been reported from the MC adjoining the PB.

2.2. Local Geology

The present study area lies in the southern part of the PB basin (Fig. 1c and d), which forms an antiformal structure overturned toward west with its closure towards NE of Samarkiya (Figs. 1c, 2a and b). The area comprises deformed and foliated garnetiferous metapelites belonging to the Potla Formation of the basement MC, which is unconformably overlain by basal quartzite of the PB Group (Figs. 1d and 2c). The basal part of the Pur Formation is represented by the Pur quartzite (PQ), which is commonly massive to micaceous and locally conglomeratic in nature

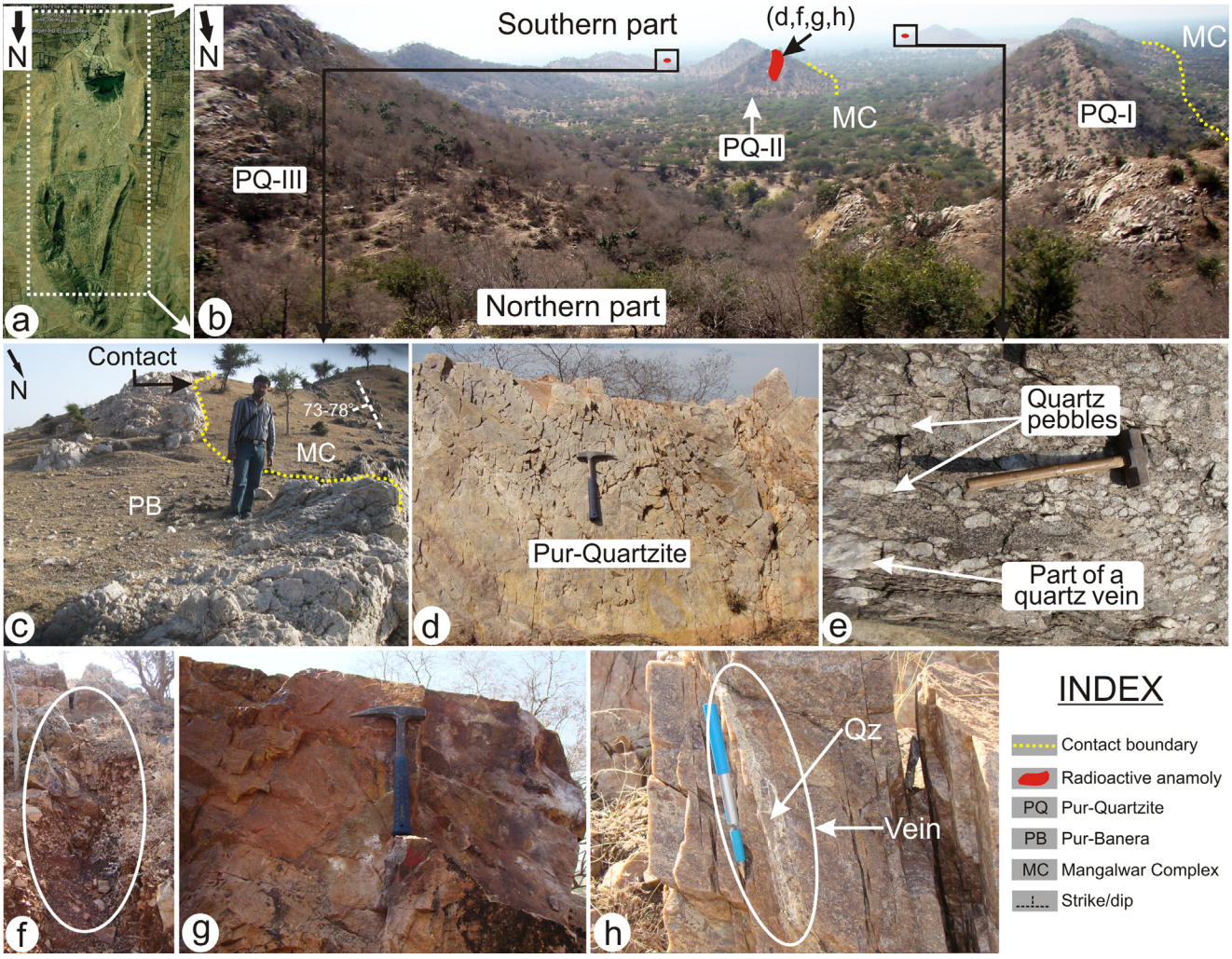

Fig. 2. Aerial (a) and panoramic view (b) of the Samarkiya antiform and field photographs (c–h) showing different litho units; (c) contact between the rocks of the Mangalwar Complex (MC) and the Pur-Banera (PB); (d) and (e) are massive Pur quartzite and its conglomeratic parts respectively; (f), (g) and (h) respectively are brecciated radioactive Pur quartzite, massive Pur quartzite, and brecciated vein, comprising predominantly of illite and quartz fragments in Pur quartzite.

(Fig. 2d and e). The exposed quartzite in the area occurs mostly as weather resistant ridges forming the Samarkiya hill, whereas the basement (i.e., MC rocks) lies in the valley trending NNE in general with steeply dipping (73–78° towards east) foliation plane (Fig. 2b and c). The Pur quartzite is greyish to light brown in color (Fig. 2d) and exposed intermittently as three isolated outcrops (PQ-I, II, and III in Fig. 2b), of variable width (200–500 m) and steep NNE trending bedding planes. The contact of the quartzite with the basement is locally marked by pods/sacks of massive, fractured, brecciated, and highly silicified quartzite (Figs. 1d, 2c and f), which are pink to brown in color (Fig. 2g). Intense fracturing and hydrothermal activity associated with vein development is exhibited by quartzite (Fig. 2h) and occasionally by conglomerate (Fig. 2e).

Shaji et al. (2007) reported surficial radioactive anomaly from the Samarkiya area in the basal Pur quartzite, which lies within four sub-parallel bands ranging in length from 50 to 320 m, and width varying between 0.5 and 2 m. Uranium mineralization is confined to the fractured and brecciated zones of the silicified quartzite (Fig. 2f and g) in PQ-II, while the foliated and the conglomeratic parts are barren. The highest radioactive anomaly is reported from the PQ-II outcrop, and accordingly six boreholes were drilled by AMDER on this outcrop (Fig. 1c and d). Further, local radioactive anomalies were noted in the southernmost part of the PQ-I and PQ-III outcrop (Fig. 2b). Based on XRD studies, Shaji et al. (2007) identified uranium minerals such as uraninite, brannerite, uranophane, carnotite, kasolite and masuyite from the PQ-II outcrop. On the contrary, the exposed MC rocks in the area are devoid of anomalous radioactivity.

3. Methodology and analytical conditions

Systematic sampling along and across the strike length of radioactive bands/lenses were carried out in the fractured and fresh exposures of the Pur quartzite. Hand-held thallium-doped NaI (Tl) scintillation counter was used to detect radioactivity of the samples in the field. Based on higher radioactivity recorded by scintillation counter, a few hand specimens from the exposed Pur quartzite (as shown by red colored zones in Fig. 2b), and one from the drill core (SMK5, Fig. 1c and d) were collected. Polished thin sections were prepared for optical microscopic and back-scattered electron (BSE) imaging studies. Subsequently, few samples were selected for electron probe micro (EPM) analyses of uranium-bearing minerals and chemical dating of uraninite.

BSE imaging and preliminary semi-quantitative energy dispersive spectroscopic (EDS) analyses were carried out with the help of a JEOL JSM 6490 scanning electron microscope (SEM). Major

(U, Pb, Th, and Y), minor (Si, Fe, K, Ca, Al, and Na), and trace (La, Ce, Pr, Nd, Sm, Eu, Gd, Dy, Ho, Er, Yb, and Lu) element analyses of uraninite were carried out using a Cameca SX-100 EPMA equipped with four wavelength dispersive spectrometers (WDS). Four different crystals were used: thallium acid phthalate (TAP in WDS 1), lithium fluoride (LIF in WDS 2), large pentaerythritol [LPET crystal (in WDS 3)], and PET (in WDS 4). CAMECA SX-100 software was used for calibration, overlap correction, quantification, and age calculations. High-resolution X-ray element maps for Y, Th, U, Si, and Pb of the uraninite grains were obtained in the same instrument. Uraninite spot analyses were performed at acceleration voltage of 20 kV, beam current of 40 nA, and beam size of 1 μm using a LaB_6 electron source. High-resolution WDS scans were performed in various uraninite grains prior to calibration to identify all the possible elements present and to monitor the spectral interferences of elements of interest. Accordingly, accurate background positions were calculated for respective elements. Special care was taken during selection of background positions for the REEs due to many possible cross-interferences. Both natural and synthetic reference materials were used for calibration. The details of analyzed line, analytical time, background positions, standards, and detection limits are provided in Supplementary Appendix A1. For background measurement of Pb Mα line, the exponential background fit was adopted to the curvature of the background values (Jercinovic and Williams, 2005; Williams et al., 2006, 2007). For uranium, the U M_β line was preferred over the U M_α line to avoid interference of the latter with Th M_α (Suzuki and Kato, 2008). During quantification, small overlapping corrections of Y $L\gamma_2$, Y $L\gamma_3$ lines of yttrium on Pb M_α and Th Mγ, Th M_3N_4 of Th on U M_β, Ho L_n on Gd L_β, Sm $L\gamma_3$ on Ho L_β, Eu $L_{\beta7}$ on Er L_α, and Nd L_α on La L_α were corrected by using the Peak Sight Software in-built in CAMECA SX-100. X-ray imaging was carried out at accelerating voltage of 15 kV and a beam current of 150 nA with 100 ms dwell time at 0.2–0.6 μm step length depending upon the grain size. It should be noted that, several studies were conducted on REE geochemistry of uraninite using secondary ion mass spectrometer (SIMS; e.g., Bonhoure, 2007) and laser ablation inductively coupled mass spectrometer (LA-ICP-MS; e.g., Mercadier et al., 2011; Eglinger at al., 2013; Frimmel et al., 2014; Alexandre et al., 2015), whereas the usage of EPMA for such studies are very scanty (e.g., Pal and Rhede, 2013; Macmillan et al., 2016; Mukhopadhyay et al., 2016). In the present study, small grain size (maximum 60 μm) of the uraninites in the samples hindered us to perform LA-ICP-MS analysis for quantifying the distribution of the REEs within the grains. Therefore, the same was undertaken using EPMA, wherein the REEs were analyzed using LIF and LPET crystals with high counting time (i.e., 40–60 and 20–30 s) for the peak and the background, respectively (Supplementary Appendix A1). The concentrations of Eu and Lu in all the analyzed uraninites are below detection limit (bdl), thus not included in the data (see Table 2, Supplementary Appendices A2 and A3).

4. Description of host rocks and modes of occurrence of uraninite

4.1. Basement (MC)

The exposed MC rocks constitute deformed and metamorphosed garnetiferous metapelites (Fig. 2c) comprising predominantly of quartz, biotite, muscovite, chlorite, garnet, plagioclase, staurolite, and kyanite as major phases (Fig. 3a). Although these rocks contain radioactive minerals like zircon and monazite as accessory phases (Ozha et al., 2016a), none of them exhibits anomalous radioactivity in the field probably due to the low abundance of these minerals and absence of uraninite. On the contrary, the sub-surface drill core sample belonging to the MC, collected from a depth of 127 m from the bore hole #SMK5 (25°12′38.2″N, 74°27′16.8″E; Fig. 1c and d) exhibits high radioactivity. In addition to the common minerals found in the exposed MC, the drill core sample also contains K-feldspar, sericite, clay (illite), apatite, uraninite, xenotime, and thorite (Fig. 3b). Additionally an unidentified LREE-bearing phase (Fig. 3d, f, and g) and rare coffinite (Fig. 3c) occur in these samples. The pervasive foliation is defined by oriented flakes of biotite and muscovite that commonly warp around garnet (Fig. 3a). The major minerals (i.e., biotite, plagioclase, kyanite, garnet, muscovite, and quartz) in the exposed sample represent the peak metamorphic assemblage for the last metamorphic event at ~0.99 Ga (Ozha et al., 2016a).

Uraninite grains are ~5 to ~50 μm in size, euhedral to anhedral in shape and occur as inclusions in the major minerals, viz. plagioclase, biotite, chlorite and quartz (Fig. 3c–h). Uraninite at places is closely associated with REE-minerals (Fig. 3g and h). Based on the shape, relative position with respect to the grain boundary of the host mineral and textural relations with the REE-bearing minerals, uraninite inclusions are classified into three different groups that define three different compositional types (see section on geochemistry of uraninite below). These are (1) $U_{MC\text{-}1}$: anhedral to subhedral inclusions, well inside the host mineral (Fig. 3c–e); (2) $U_{MC\text{-}2}$: subhedral to euhedral inclusions at the grain boundary of the host mineral (Fig. 3f); (3) $U_{MC\text{-}3}$: anhedral inclusions rimmed and/or replaced by REE-minerals, viz. monazite and xenotime (Fig. 3g and h; See Table 1 for a summary of textures, compositions and ages). At places, $U_{MC\text{-}1}$ uraninites show different gray shades in BSE image indicating intra-grain compositional heterogeneity (Fig. 5g; see section on uraninite geochemistry).

The rock (#SMK5) as such does not have any evidence of large-scale alteration features, presumably due to the obliteration of such features, if any, during subsequent metamorphism. However, uraninite grains included in plagioclase commonly show circular radiation damage-controlled alteration halos (Fig. 3c, d, f and h). Based on the distribution, texture and composition of the alteration minerals, Ozha et al. (2016b) proposed a post-mineralization sequential alteration in which plagioclase was replaced by K-feldspar, and K-feldspar in turn was replaced by clay mineral (i.e., illite) implying an acidic alteration following potassic alteration. In addition to the common presence of large biotite that defines foliation, small flakes and irregular patches of biotite appear to replace plagioclase (Fig. 3c). Chlorite replaces biotite along cleavages and grain boundaries (Fig. 3b–c, and f) and in the radiohalo zone (Fig. 3e). It is uncertain whether biotitization of plagioclase and chloritization of biotite (excepting those in the radiohalo zones) can be linked to the same post-mineralization potassic and acidic alteration as observed in the alteration halo. Presence of unidentified REE-bearing phases (Fig. 3c–d, f and h) in the alteration halo suggests introduction or re-distribution of REEs, at least in the micro-domain scale during such post-mineralization alteration. It is uncertain whether the discrete REE-bearing phases that are associated with $U_{MC\text{-}3}$ uraninite formed during this stage.

4.2. Supracrustals (PB)

The Pur quartzite shows variable surface radioactive anomalies restricted to the silicified quartzite, in which the mineralization is disseminated and localized, with a very poor lateral continuity. However, high radioactivity counts are associated with the fractured, jointed and brecciated zones of the quartzite (Fig. 2f and g). Fracture-filled brecciated veins comprising quartzite fragments in illite matrix, were occasionally encountered (Figs. 2h and 4f) in the PQ-II outcrop. Accordingly, samples were collected from various sites of the quartzite with high radioactivity counts (as shown in Fig. 2b). The Pur quartzite is composed domi-

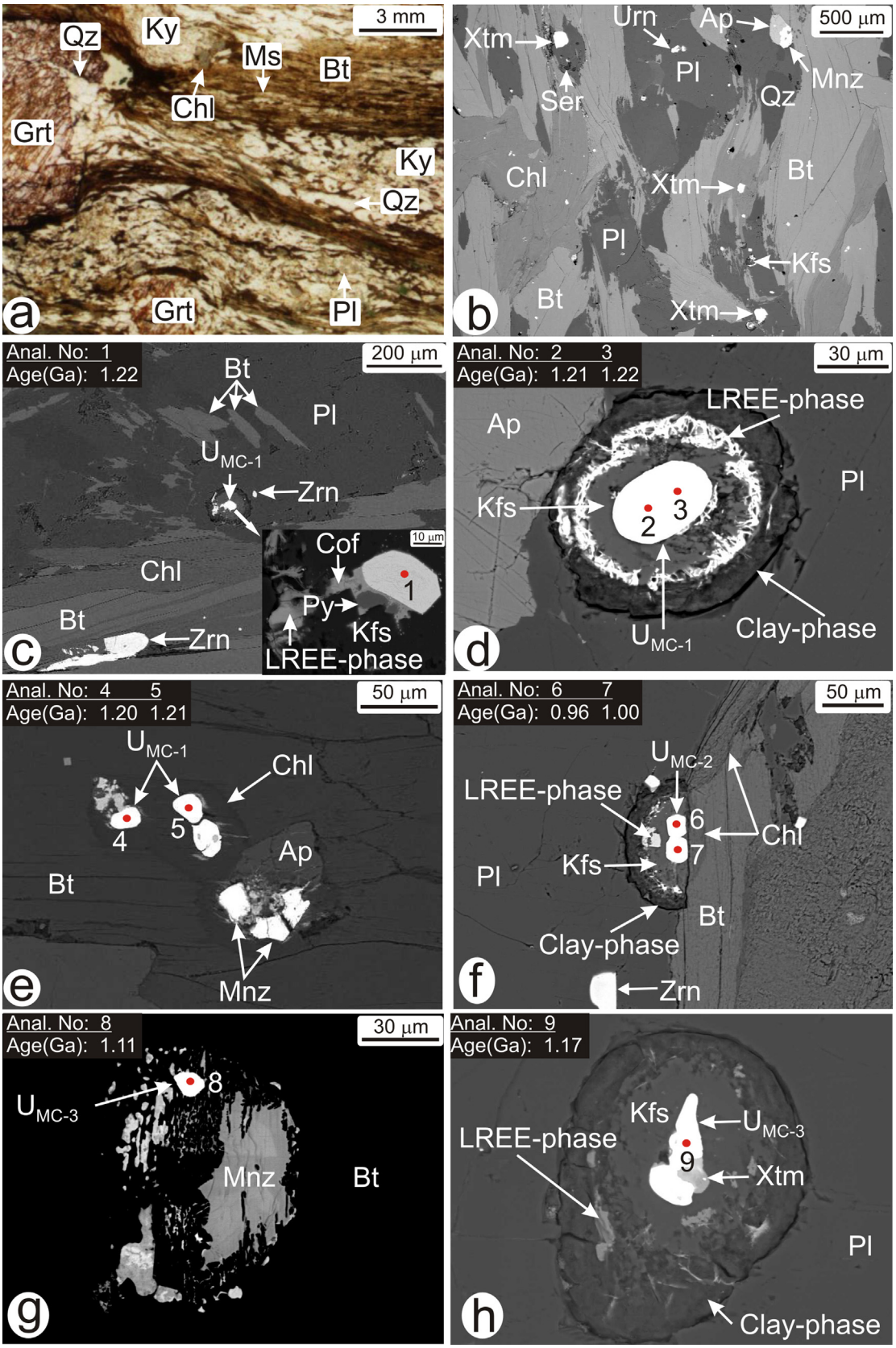

Fig. 3. Representative photomicrograph (a) and back-scattered electrons images (BSE; b through h) showing overall rock fabric and documenting modes of occurrence of uraninite respectively in the basement Mangalwar Complex; (a) the host rock containing garnet, quartz, kyanite, plagioclase, chlorite, biotite, and muscovite, where biotite and muscovite define the schistosity; (b) general distribution of uraninite, xenotime, and monazite; uraninites occur well within host minerals (U_{MC-1}) viz. plagioclase (c–d) and biotite (e), at or close to the grain boundaries (U_{MC-2}) of these minerals (f) and at places associated with and replaced by REE-bearing phases (U_{MC-3}; g–h). Note that the uraninite inclusions in plagioclase are invariably surrounded by alteration halos filled with K-feldspar, LREE-phase, and clay in host plagioclase while the halo in biotite is represented by chlorite. Also note that patchy biotite and chlorite replaces plagioclase and biotite respectively (c). Numerals in this and subsequent figures correspond to analysis numbers and ages, given in Table 2. Mineral abbreviations in this and other figures are after Whitney and Evans (2010). See text for discussion.

Table 1
Summary of different textural and compositional classifications of uraninite and their corresponding ages from the basement and the supracrustal rocks.

	Textural classification	Textural description	Composition	Compositional classification		Age	Sketch of uraninite texture
Basement	U_{MC-1} (Fig. 3c–e)	Isolated and well inside the host mineral	Nearly pure uraninite with very low content of Y + REEs and minor elements	High PbO	[a]MC_{G-1a}	1196 ± 5	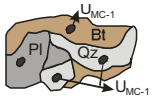
	U_{MC-2} (Fig. 3f)	Isolated and at the grain boundary		Low PbO	MC_{G-1b}	955 ± 6 Ma	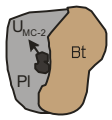
	U_{MC-3} (Fig. 3g–h)	Rimmed/replaced by REE-bearing minerals	Elevated contents of Y + REEs	Variable PbO	MC_{G-2}	Variable; extrapolated age considering Y + REEs to be zero is 1220 ± 14	
Supracrustal	U_{PB-1} (Fig. 4b–d)	Isolated and well inside the host mineral	Nearly pure uraninite with very low content of REEs and minor elements	High PbO	PB_{G-1a}	1239 ± 5	
	U_{PB-2} (Fig. 4b–d)	Isolated and at the grain boundary or connected to the grain boundary of the host through micro-cracks		Low PbO	PB_{G-1b}	1006 ± 7	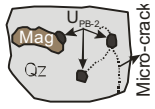
	U_{PB-3} (Fig. 6g–h)	Rimmed/replaced by U-silicates	Elevated content of minor elements	Variable PbO	[b]PB_{G-2}	Variable: extrapolated age considering minor elements to be zero is 1211 ± 27	

[a] some U_{MC-1} grains are chemically heterogeneous, wherein the fresh and altered parts respectively are MC_{G-1a} and MC_{G-2} in composition (Fig. 5g).
[b] some U_{PB-3} grains are chemically heterogeneous, wherein the fresh and altered parts respectively are U_{PB-1a} and U_{PB-2} in composition (Fig. 6g); in addition remnants of PB_{G-1a} and new PB_{G-2} (Fig 6h-i) occur in some association.

nantly of quartz, with minor/accessory phases such as muscovite, garnet, biotite, chlorite, zircon, and rare monazite.

Quartzite from the vicinity of the brecciated zones (Fig. 2f and g) contains strained and elongated quartz with sutured grain contact and sporadic biotite, muscovite, chlorite, and garnet (Fig. 4a and b). These samples contain radioactive uraninite, coffinite and uranophane (Figs. 4b–d and 6g–i). Non-radioactive ore minerals include magnetite (replaced by hematite; Fig. 4e), pyrite, and galena (Fig. 6h–i). The quartzite sample, collected from close to the brecciated vein (Fig. 2h) contains U-bearing phases in the wall rock quartzite (Fig. 4g and h), and in the fragments of quartzite enclosed in the veins (Fig. 4f), whereas the vein containing illite is devoid of these phases (Fig. 4f). Unlike the common presence of the REE-phases, viz. monazite, xenotime and unidentified REE-minerals in the basement, commonly coffinite and at places uranophane are associated with uraninite in the supracrustal rocks.

Similar to the basement rocks, the supracrustal uraninite also occurs as inclusions in different minerals. However, based on their shape, position with respect to the grain boundary of the host mineral and association with U-silicate minerals, uraninite inclusions are classified into three different types. These are (1) U_{PB-1}: anhedral to subhedral inclusions well inside the host mineral (Fig. 4b–d); (2) U_{PB-2}: subhedral to euhedral inclusions at the grain boundary and/or closely associated with micro-cracks (Fig. 4c–d and 4g–h); (3) U_{PB-3}: commonly anhedral inclusions rimmed and partly replaced by U-silicates such as coffinite and uranophane (Fig. 6g–i; See Table 1 for a summary of texture, composition and ages). U_{PB-1} uraninites are included in quartz (Fig. 4c–d and 4f–h) and magnetite (Fig. 4b), the latter at places is partly included in garnet. Some large U_{PB-3} uraninite show different gray shades in BSE image suggesting intra-grain compositional variation (Fig. 6g; see section on uraninite geochemistry).

Unlike the basement rocks, the studied PB rocks do not show any evidence either of large-scale/micron-scale alteration, presumably due to the fact they are composed primarily of quartz. However, the rocks were subjected to silicification and K^+/H^+ metasomatism as evident from the presence of quartz and illite veins.

5. Geochemistry of uraninite

Uraninite occurs as inclusions in different minerals and host rocks in the basement and the supracrustal. It is therefore necessary to recognize the differences, if any, in the compositions between uraninites of the basement and supracrustal. In this section, we first describe the general geochemical character of uraninites and then geochemistry of different textural types. As BSE images indicate possible compositional variations in individual grains, we examine such intra-grain compositional variations in the context of general compositional characteristics vis-à-vis textures of uraninite. Representative compositional data of uraninite from the basement and the supracrustals rocks are presented in Table 2 and complete analytical data are given in Supplementary Appendices A2 and A3.

5.1. Uraninite in the basement: Inter- and intra-granular variations

A total of 99 EPM analyses were obtained from 65 basement uraninite grains and all the compositional data are presented in Supplementary Appendix A2. The obtained total elemental oxide content of these grains is mostly ~100, while few spots exhibit a lower total (with a minimum value of 96.49). Low totals may be attributed to the presence of U^{+6} in the structure of uraninite, alteration/hydration and development of pores, and also to the presence of elements which were not analyzed (e.g., Pal and Rhede, 2013; Frimmel et al., 2014). Near 100 totals in most grains indicates, even if present, U^{+6} contents in the studied uraninites are negligible and therefore self-oxidation due to radioactive decay

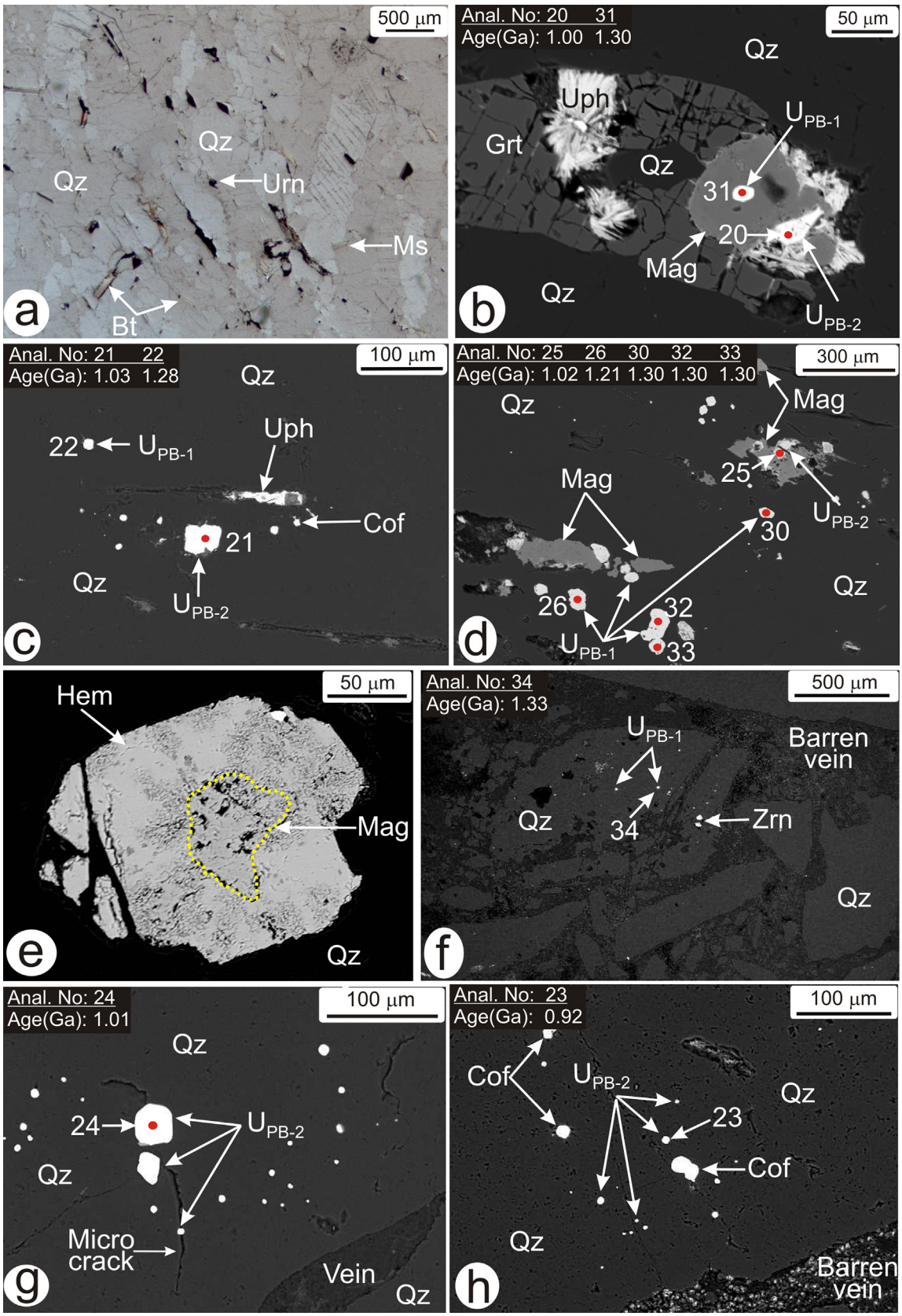

Fig. 4. Photomicrograph (a) and BSE images illustrating textural relationship of uraninite within the brecciated quartzite (b–e) and fracture filling vein (f–h) from the Pur quartzite. Uraninite occurs within (U_{PB-1}) and at the contact of (U_{PB-2}) magnetite and quartz (b–d); hematite formed after magnetite (e); note that the fracture filling vein is barren (f) while uraninite (U_{PB-1} and U_{PB-2}) occurs in the fragments of quartzite (f–h); coffinite and uranophane are found in the vicinity of uraninite (in b, c, and h) but do not appear to have replaced uraninite.

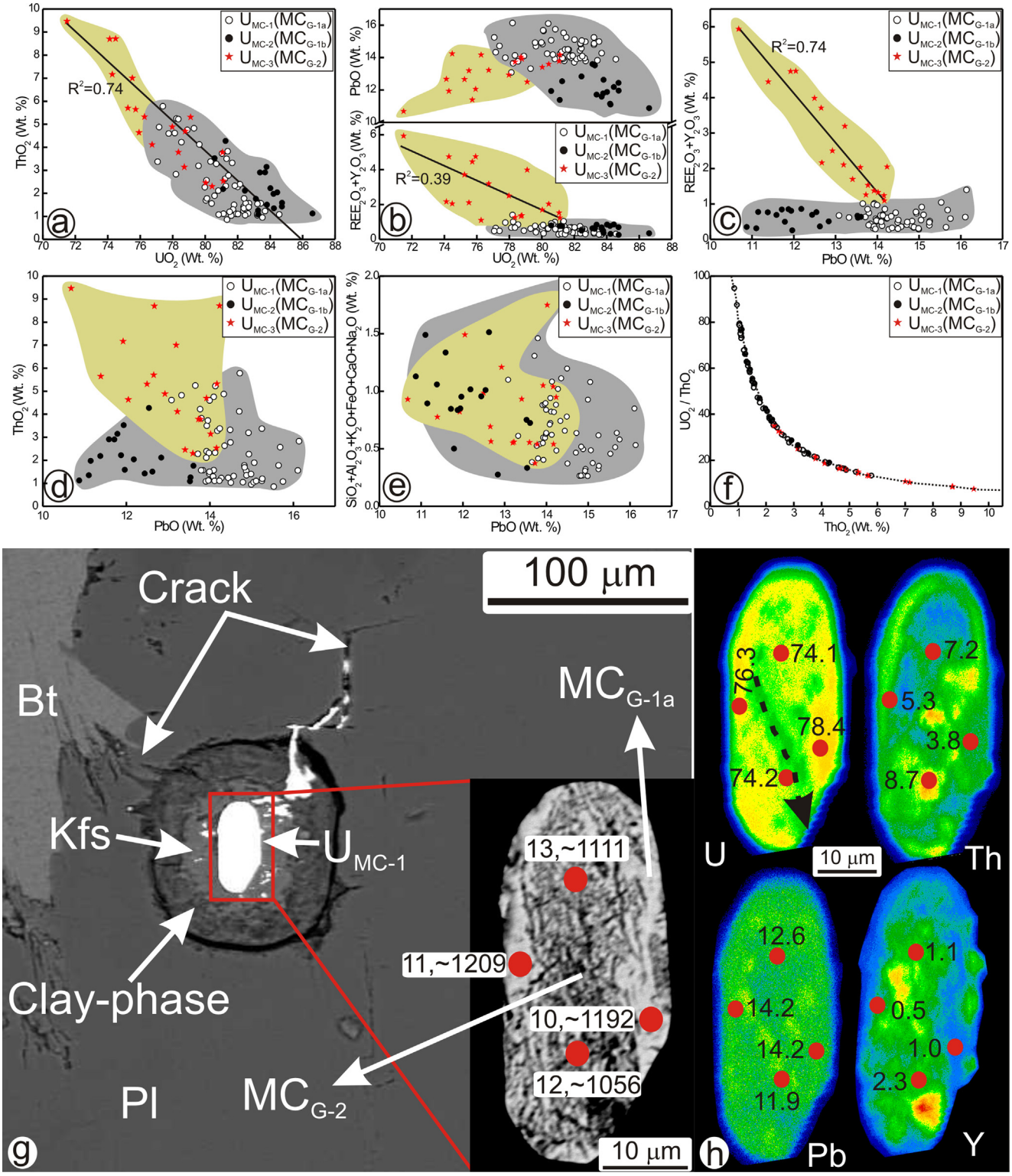

Fig. 5. Concentrations (in oxide wt%) of different major, minor and trace elements of different textural types in the basement uraninite (a through f). The major compositional types corresponding to each textural type are shown in parentheses. Although texturally different uraninites are indistinguishable from each other in terms of total minor element content (e), $U_{MC\text{-}1}$ and $U_{MC\text{-}2}$ uraninites are depleted in $\sum REY_2O_3$ compared to $U_{MC\text{-}3}$ and define a populations (marked by grey shade; compositional type $MC_{G\text{-}1}$) distinctly different from $U_{MC\text{-}3}$ (marked by yellow shade; compositional type $MC_{G\text{-}2}$) (c). Note that $U_{MC\text{-}1}$ is characteristically more enriched in PbO compared $U_{MC\text{-}2}$ (b to e) and thus define two compositional populations namely $MC_{G\text{-}1a}$ and $MC_{G\text{-}1b}$. SEM-BSE image (g) and X-ray element maps (h) of a plagioclase-hosted large uraninite grain, connected to the grain boundary through micro-cracks and surrounded by alteration halo, exhibits intra-granular compositional difference. The uraninite in (g) texturally belongs to the $U_{MC\text{-}1}$, but represents two compositional types, $MC_{G\text{-}1a}$ and $MC_{G\text{-}2}$.

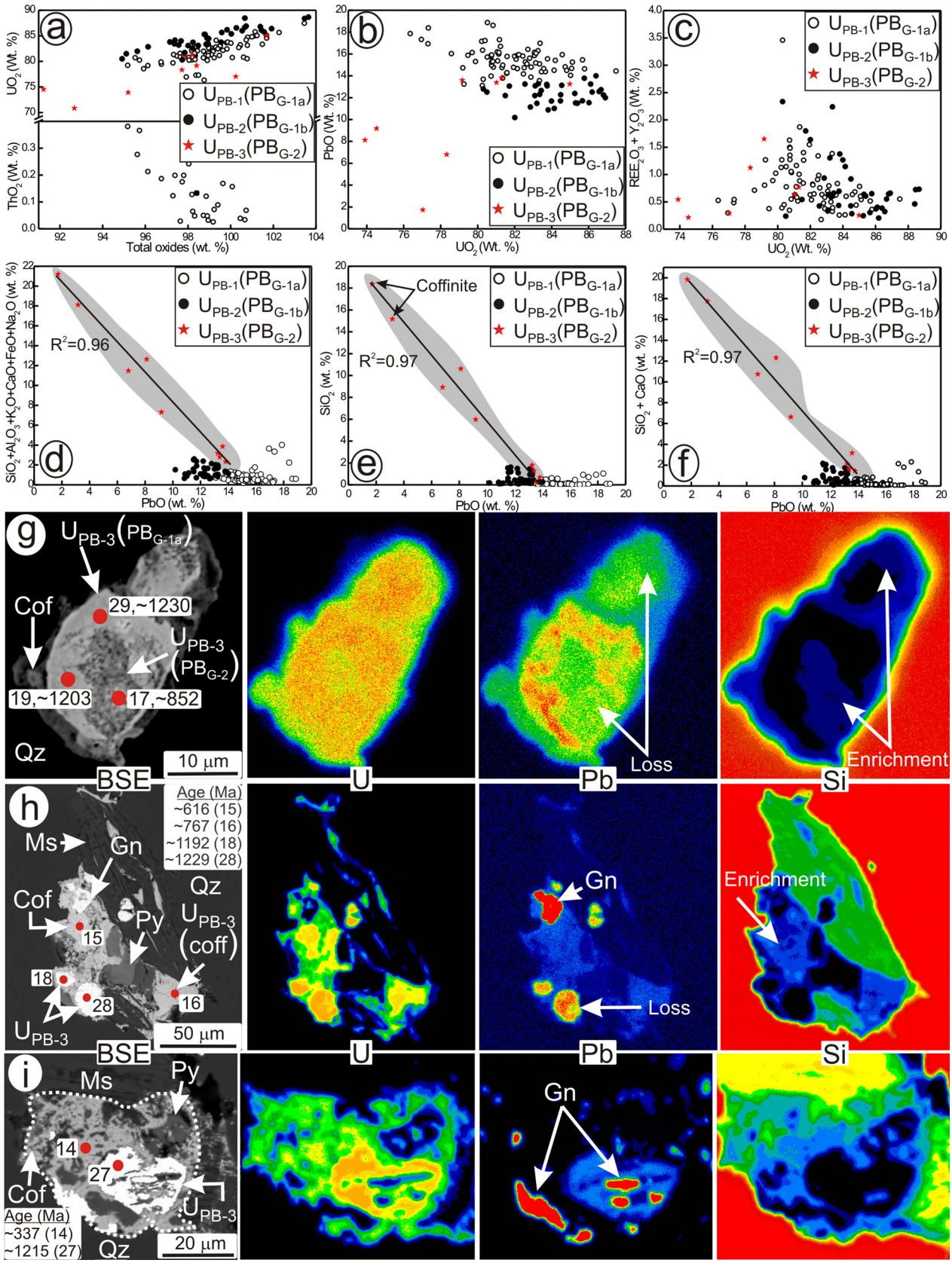

Fig. 6. Concentrations (in oxide wt%) of different major, minor and trace elements of different textural types in the supracrustal uraninite (a through f). The major compositional types corresponding to each textural type are shown in parentheses. Even though texturally different uraninites are indistinguishable from each other in terms of $\sum REY_2O_3$ content, some U_{PB-3} uraninites contain much elevated concentrations of minor elements (compositionally PB_{G-2}) compared to U_{PB-1} and U_{PB-2} (compositionally PB_{G-1}) that shows strong negative correlations with PbO (d–f). Note that the U_{PB-1} uraninites are enriched in PbO than U_{PB-2} and define two compositional groups namely PB_{G-1a} and PB_{G-1b} (b, d–f). BSE images and X-ray element maps of three large uraninite grains associated with and partly replaced by coffinite (g–i) show intra-grain compositional heterogeneity, preserving both PB_{G-1a} and PB_{G-2} compositions (g), presence of two compositional types (PB_{G-1a} and PB_{G-2}) of uraninite (h) and also retention of earlier compositions (PB_{G-1a}) in the remnants of earlier grain (h and i).

Table 2
Representative mineral composition with respective calculated chemical ages for the Basement (Mangalwar Complex) and supracrustal (Pur-Banera) rocks.

Basement (Mangalwar Complex)													
Figure	3c	3d	3d	3e	3e	3f	3f	3 g	3 h	5 g	5 g	5 g	5 g
Mineral	Urn	Urn	Urn	Urn	Urn	Urn	Urn	Urn	Urn	Urn	Urn	Urn	Urn
Texture	U_{MC-1}	U_{MC-1}	U_{MC-1}	U_{MC-1}	U_{MC-1}	U_{MC-2}	U_{MC-2}	U_{MC-3}	U_{MC-3}	U_{MC-1}	U_{MC-1}	U_{MC-1}	U_{MC-1}
Composition	MC_{G-1a}	MC_{G-1a}	MC_{G-1a}	MC_{G-1a}	MC_{G-1a}	MC_{G-1b}	MC_{G-1b}	MC_{G-2}	MC_{G-2}	MC_{G-1a}	MC_{G-1a}	MC_{G-2}	MC_{G-2}
Analysis No.	1	2	3	4	5	6	7	8	9	10	11	12	13
SiO_2	0.12	0.08	0.12	bdl	0.09	bdl	0.13	0.05	0.79	0.11	bdl	bdl	0.07
Al_2O_3	bdl	bdl	bdl	bdl	bdl	bdl	bdl	bdl	0.33	bdl	0.03	bdl	bdl
CaO	0.1	0.05	0.1	0.07	0.2	0.16	0.12	0.08	0.37	0.29	bdl	0.09	bdl
FeO	bdl	bdl	bdl	bdl	0.47	0.5	0.26	0.15	bdl	0.28	0.29	0.56	0.23
Na_2O	bdl	bdl	bdl	bdl	bdl	0.04	0.07	bdl	0.07	bdl	bdl	bdl	bdl
K_2O	0.16	0.19	0.16	0.19	0.3	0.29	0.27	0.26	0.19	0.27	0.25	0.18	0.25
Y_2O_3	0.15	0.12	0.15	0.1	0.08	0.11	0.23	0.33	0.44	0.97	0.45	2.3	1.06
La_2O_3	bdl	bdl	bdl	bdl	bdl	bdl	bdl	0.42	bdl	bdl	bdl	bdl	bdl
Ce_2O_3	bdl	bdl	bdl	bdl	bdl	bdl	bdl	0.14	bdl	0.01	bdl	bdl	bdl
Pr_2O_3	bdl	bdl	bdl	bdl	0.43	0.15	0.3	0.33	bdl	0.43	0.39	bdl	0.39
Nd_2O_3	bdl	0.14	bdl	bdl	bdl	bdl	bdl	0.31	0.2	0.15	bdl	0.18	bdl
SmO	bdl	bdl	bdl	bdl	bdl	bdl	bdl	bdl	bdl	bdl	bdl	0.24	bdl
Gd_2O_3	0.32	bdl	0.32	bdl	bdl	bdl	0.2	bdl	0.31	0.23	bdl	0.6	0.13
Dy_2O_3	bdl	bdl	bdl	bdl	bdl	bdl	0.07	bdl	0.14	0.17	0.06	0.63	0.29
Ho_2O_3	0.22	0.14	0.22	0.21	bdl	bdl	bdl	bdl	0.24	bdl	bdl	0.26	bdl
Er_2O_3	bdl	bdl	bdl	bdl	bdl	bdl	bdl	bdl	bdl	bdl	0.08	0.28	0.18
Yb_2O_3	bdl	bdl	bdl	bdl	bdl	bdl	bdl	bdl	bdl	bdl	bdl	0.26	0.11
UO_2	82.21	83.21	82.02	82.69	82.46	84.73	80.57	81.07	78.71	78.35	76.26	74.28	74.12
ThO_2	1.11	1.11	1.1	1.4	1.05	1.59	3.53	3.77	3.14	3.78	5.32	7.16	8.69
PbO	15.11	15.25	15.11	14.99	15.05	11.96	11.94	13.8	13.9	14.23	14.17	11.93	12.67
Total	99.29	100.3	99.6	99.85	100.2	99.61	97.77	100.7	98.8	99.44	97.38	98.98	98.33
Minors	0.38	0.32	0.38	0.26	1.06	0.99	0.85	0.54	1.75	0.95	0.57	0.83	0.55
SiO_2 + CaO	0.21	0.13	0.22	0.07	0.29	0.16	0.25	0.13	1.15	0.4	bdl	0.09	0.07
ΣREE_2O_3	0.55	0.28	0.54	0.21	0.43	0.15	0.57	1.2	0.89	0.99	0.53	2.45	1.1
$\Sigma LREE_2O_3$	bdl	0.14	bdl	bdl	0.43	0.15	0.3	1.2	0.2	0.59	0.39	0.42	0.39
$\Sigma HREE_2O_3$	0.55	0.14	0.54	0.21	bdl	bdl	0.27	0	0.69	0.4	0.14	2.03	0.71
$\Sigma REE_2O_3 + Y_2O_3$	0.7	0.4	0.69	0.31	0.51	0.26	0.8	1.53	1.33	1.96	0.98	4.75	2.16
Age (Ma)	1217	1212	1217	1199	1207	959	996	1125	1167	1192	1209	1056	1111
2 s error (Ma)	25	24	25	24	35	28	29	33	24	34	35	23	32

(*continued on next page*)

Table 2 (*continued*)

Supracrustal (Pur-Banera)																					
Figure	6i	6 h	6 h	6 g	6 h	6 g	4b	4c	4c	4 h	4 g	4d	4d	6i	6 h	6 g	4d	4b	4b	4d	4f
Mineral	Cof	Urn	Urn	Urn	Urn	Urn	Urn	Urn	Urn	Urn	Urn	Urn	Urn	Urn	Urn	Urn	Urn	Urn	Urn	Urn	Urn
Texture	–	U_{PB-3}	U_{PB-3}	U_{PB-3}	U_{PB-3}	U_{PB-3}	U_{PB-2}	U_{PB-2}	U_{PB-1}	U_{PB-2}	U_{PB-2}	U_{PB-2}	U_{PB-1}	U_{PB-3}	U_{PB-3}	U_{PB-3}	U_{PB-1}	U_{PB-1}	U_{PB-1}	U_{PB-1}	U_{PB-1}
Composition		PB_{G-2}	PB_{G-2}	PB_{G-2}	PB_{G-1a}	PB_{G-1a}	PB_{G-1b}	PB_{G-1a}	PB_{G-1a}	PB_{G-1b}	PB_{G-1b}	PB_{G-1b}	PB_{G-1a}	PB_{G-1a}	PB_{G-1a}	PB_{G-1a}	PB_{G-1a}	PB_{G-1a}	PB_{G-1a}	PB_{G-1a}	PB_{G-1a}
Analysis No.	14	15	16	17	18	19	20	21	22	23	24	25	26	27	28	29	30	31	32	33	34
SiO_2	15.16	8.92	10.61	0.43	0.11	bdl	0.28	0.24	bdl	1.13	0.16	0.13	0.56	0.18	0.04	0.07	bdl	0.08	0.08	0.04	0.45
Al_2O_3	bdl	0.15	bdl	bdl	bdl	bdl	bdl	bdl	bdl	bdl	bdl	bdl	bdl	bdl	bdl	bdl	bdl	bdl	bdl	bdl	0.06
CaO	2.59	1.83	1.7	0.76	0.1	bdl	0.09	0.04	0.05	0.9	0.09	0.05	0.28	0.27	0.11	bdl	0.10	0.07	0.06	0.15	0.12
FeO	bdl	0.18	bdl	0.14	bdl	bdl	bdl	bdl	bdl	0.25	0.31	bdl	bdl	0.19	0.05	bdl	1.38	0.03	0.01	bdl	bdl
Na_2O	0.08	0.11	0.06	0.2	0.26	bdl	0.04	0.06	bdl	0.06	0.2	0.02	bdl	bdl	0.07	bdl	bdl	bdl	0.18	bdl	0.15
K_2O	0.28	0.28	0.26	0.29	0.3	0.18	0.3	0.29	0.29	0.28	0.29	0.7	0.2	0.28	0.29	0.21	0.28	0.27	0.3	0.28	0.29
Y_2O_3	bdl	bdl	bdl	0.43	bdl	0.08	0.12	0.2	0.11	0.07	0.11	0.08	bdl	0.37	0.44	bdl	0.27	0.05	0.15	0.26	bdl
La_2O_3	bdl	0.26	0.07	bdl	bdl	bdl	bdl	bdl	bdl	bdl	bdl	bdl	bdl	bdl	bdl	bdl	bdl	bdl	bdl	bdl	bdl
Ce_2O_3	0.37	0.53	0.13	0.01	0.01	bdl	0.01	bdl	bdl	bdl	bdl	0.02	bdl	0.04	bdl	bdl	0.05	bdl	bdl	bdl	bdl
Pr_2O_3	0.2	0.21	0.34	0.61	0.31	bdl	0.28	0.46	0.43	0.3	0.41	0.34	bdl	0.5	0.51	bdl	0.61	0.43	0.38	0.42	0.31
Nd_2O_3	bdl	0.12	bdl	0.1	0.23	bdl	0.15	bdl	bdl	bdl	bdl	bdl	bdl	bdl	0.18	bdl	0.27	0.13	0.11	0.23	0.08
SmO	bdl	bdl	bdl	bdl	bdl	bdl	bdl	bdl	bdl	bdl	bdl	bdl	bdl	bdl	bdl	bdl	0.11	bdl	bdl	bdl	bdl
Gd_2O_3	0.08	bdl	bdl	0.24	bdl	bdl	bdl	bdl	0.11	bdl	0.21	0.12	bdl	0.12	0.22	bdl	0.08	0.18	bdl	0.25	bdl
Dy_2O_3	bdl	bdl	bdl	0.13	bdl	bdl	bdl	bdl	bdl	bdl	bdl	bdl	bdl	bdl	bdl	bdl	bdl	bdl	bdl	bdl	bdl
Ho_2O_3	bdl	bdl	bdl	bdl	bdl	0.25	bdl	bdl	bdl	bdl	bdl	bdl	0.18	bdl	bdl	0.26	bdl	bdl	bdl	bdl	bdl
Er_2O_3	bdl	bdl	bdl	bdl	bdl	bdl	bdl	bdl	bdl	bdl	bdl	bdl	bdl	bdl	bdl	bdl	0.10	bdl	bdl	bdl	bdl
Yb_2O_3	bdl	bdl	bdl	bdl	bdl	bdl	bdl	bdl	bdl	bdl	bdl	bdl	bdl	bdl	bdl	bdl	bdl	bdl	bdl	bdl	bdl
UO_2	70.83	78.32	73.9	85.63	85.12	83.34	86.67	83.44	82.22	86.02	88.66	81.49	82.66	80.85	80.75	83.78	80.76	81.14	82.71	81.15	80.26
ThO_2	bdl	bdl	bdl	0.03	bdl	bdl	0.03	bdl	bdl	bdl	bdl	bdl	bdl	0.03	0.2	bdl	0.16	bdl	bdl	0.03	bdl
PbO	3.17	6.8	8.12	9.95	15.25	15.09	12.74	12.65	15.94	11.54	13.2	12.2	15.09	14.8	14.99	15.56	15.92	16	16.42	16.13	16.34
Total	92.87	97.84	95.26	98.94	101.8	99.07	100.8	97.4	99.1	100.5	103.7	95.18	99.09	97.76	97.94	100.3	100.1	98.4	100.4	99.04	98
Minors	18.11	11.47	12.63	1.82	0.77	0.18	0.71	0.62	0.34	2.61	1.05	0.9	1.04	0.92	0.56	0.28	1.76	0.45	0.63	0.47	1.06
$SiO_2 + CaO$	17.75	10.75	12.31	1.19	0.21	bdl	0.37	0.28	0.05	2.03	0.25	0.18	0.84	0.45	0.15	0.07	0.10	0.15	0.14	0.19	0.57
ΣREE_2O_3	0.65	1.12	0.54	1.09	0.55	0.25	0.44	0.46	0.54	0.3	0.62	0.48	0.18	0.66	0.91	0.26	1.21	0.74	0.49	0.9	0.39
$\Sigma LREE_2O_3$	0.57	1.12	0.54	0.72	0.55	bdl	0.44	0.46	0.43	0.3	0.41	0.36	bdl	0.54	0.69	bdl	1.03	0.56	0.49	0.65	0.39
$\Sigma HREE_2O_3$	0.08	bdl	bdl	0.37	bdl	0.25	bdl	bdl	0.11	bdl	0.21	0.12	0.18	0.12	0.22	0.26	0.18	0.18	bdl	0.25	bdl
$\Sigma REE_2O_3 + Y_2O_3$	0.65	1.12	0.54	1.52	0.55	0.33	0.56	0.66	0.65	0.37	0.73	0.56	0.18	1.03	1.35	0.26	1.48	0.79	0.64	1.16	0.39
Age (Ma)	327	616	767	852	1192	1203	1000	1028	1277	921	1012	1016	1212	1215	1229	1230	1295	1296	1304	1305	1332
2 s error (Ma)	7	12	15	24	20	24	18	30	36	16	18	30	24	35	35	24	37	36	22	37	22

Note: Minors = $\Sigma(SiO_2 + Al_2O_3 + CaO + Na_2O + K_2O + FeO)$; Abbreviations: Urn: Uraninite, Cof: Coffinite, bdl: Below detection limit; U_{MC-1}–U_{MC-3} and U_{PB-1}–U_{PB-3}: Texturally different uraninite; MC_{G-1a} and PB_{G-1a} etc. are different compositional types.

was minimal (Dahlkamp, 1993). Compositionally, the analyzed grains show variable contents of UO_2 (71.49–86.61 wt%), and PbO (10.68–16.14 wt%). The ThO_2 content of the grains vary from 0.86 to 9.47 wt% (Fig. 5a). Concentrations of other minor/trace elements are also variable, amongst which the content of the REEs (bdl-2.45 wt% of REE_2O_3) and Y (bdl–3.66 wt% of Y_2O_3) are substantial. Besides, minor amounts of K_2O (0.16–0.30 wt%), FeO (bdl–1.46 wt %), SiO_2 (bdl-0.79 wt%) and CaO (bdl-0.42 wt%) are detected in most cases. Very few grains have higher content of SiO_2 (4.36 wt %; See Supplementary Appendix A2) and CaO (max. 2.73 wt%). Considering that almost all uraninites in the basement contain <1.0 wt % total minor element, these stray values may appear to be the result of contamination from matrix or sub-surface inclusions. However, these grains are also enriched in REYs. Therefore, compositional modification due to alteration (discussed later) is highly possible. The concentrations of Al_2O_3 and Na_2O are below detection limits excepting in few grains (Supplementary Appendix A2). Thus, the basement uraninite grains display large variation in composition. For a better understanding on the possible reasons of such compositional variations, an assessment of the compositions of different textural types of uraninite and compositional variations within single uraninite grains (as indicated by BSE images) is necessary.

The different textural types have overlapping ranges in the concentrations of UO_2 and ThO_2 (Fig. 5a). Similarly the $\Sigma(SiO_2 + Al_2O_3 + K_2O + CaO + FeO + Na_2O)$ contents of all textural types are low and randomly distributed without forming distinct populations (Fig. 5e), Therefore concentrations of UO_2, ThO_2 and total minor elements cannot readily discriminate the different textural types. However, the $U_{MC\text{-}1}$ and $U_{MC\text{-}2}$ uraninites are characterized by very low and restricted concentrations of ΣREY_2O_3 (i.e., $\leq$1.0 wt%, excepting a couple of spots). The $U_{MC\text{-}3}$ uraninites, on the contrary, contain higher and variable concentrations of the same (ΣREY_2O_3 >1.00 to 5.93 wt%) (Fig. 5b and c). Thus, based on ΣREY_2O_3 contents uraninites in the basement can be classified into two distinct compositional groups, namely $MC_{G\text{-}1}$ (low total REY) and $MC_{G\text{-}2}$ (high total REY). Although both $U_{MC\text{-}1}$ and $U_{MC\text{-}2}$ uraninites belong to $MC_{G\text{-}1}$ compositional group, a close examination of compositions demonstrates that the $U_{MC\text{-}1}$ uraninites invariably contain higher PbO compared to the $U_{MC\text{-}2}$ uraninites. Based on these compositional variations we further divide the $MC_{G\text{-}1}$ compositional group into two subgroups namely, $MC_{G\text{-}1a}$ (low REY and high PbO; represented by $U_{MC\text{-}1}$ textural type) and $MC_{G\text{-}1b}$ (low REY and low PbO; represented by $U_{MC\text{-}2}$ textural type). Some of $U_{MC\text{-}3}$ uraninites contain higher ThO_2 compared to the $U_{MC\text{-}1}$ and $U_{MC\text{-}2}$ uraninites. The compositional relation between UO_2 and PbO illustrate two discrete populations (Fig. 5a and b), wherein the somewhat negative trend defined by $U_{MC\text{-}1}$ and $U_{MC\text{-}2}$ together (belonging to $MC_{G\text{-}1}$ compositional group) may be explained by the production of radiogenic Pb at the expense of U in a closed system. The $U_{MC\text{-}3}$ uraninites do not show any well-defined trend perhaps due to variable substitution of Pb and/or U by trace elements during subsequent processes. Although the compositional characters can largely be linked to the textures, there are deviations from this general pattern as is evident from the following description.

We have mentioned that some large uraninite grains show different grey shades in BSE images indicating compositional heterogeneity. For a better understanding on such compositional heterogeneity and its implications on the multiple compositional types described above, a representative large uraninite inclusion, belonging to the $U_{MC\text{-}1}$ textural type, (Fig. 5g) was studied integrating BSE image, X-ray element maps (U, Th, Pb, and Y; Fig. 5h) and EPM spot analysis. BSE image shows that the central channel-like part and small patches at the margin (the right margin of uraninite in Fig. 5g) is extremely fractured and dark, while the rest parts (as small patches) are smooth and bright. Note the presence of micro-cracks in the host plagioclase, some of which are extended up to the grain boundary. Although the maps do not illustrate sharp compositional zoning, significant depletion of U and Pb and enrichment of Th and Y at the fractured zones are observed. The same is confirmed by spot analysis from different zones (analyses 10, 11, 12, and 13; Table 2). It is uncertain whether the heterogeneously distributed fractured zones are the result of more radiation damage due to the elevated concentrations of radioactive elements in these zones or actually represent fluid-induced dissolution cavities. Importantly, compositions obtained from the smooth- and fractured zones are equivalent to that of $MC_{G\text{-}1a}$ and $MC_{G\text{-}2}$ respectively. Based on this intra-grain variation, we propose that the $MC_{G\text{-}2}$ compositions are the results of modification of $MC_{G\text{-}1a}$ compositions, originally displayed by $U_{MC\text{-}1}$ uraninite. Micro-cracks, extended to the grain boundary, likely acted as the fluid conduit and facilitated post-mineralization alteration. Such intra-grain compositional variations further explain why a particular textural type cannot always be uniquely linked to a particular compositional type and vice versa. Based on above discussion we propose that the $MC_{G\text{-}1a}$ and $MC_{G\text{-}1b}$ represent the pristine compositions, whereas the $MC_{G\text{-}2}$ represents the modified compositions.

5.2. Uraninite in the supracrustals: Inter- and intra-granular variation

For the supracrustal rocks, a total of 126 spot analyses were obtained from ~85 uraninite grains. Most of the analytical totals are less than or close to 100 and rarely exceed 101 (Fig. 6a; Supplementary Appendix A3). Very few grains exhibit high analytical totals (~103), which may be attributed to contamination from the host mineral or sub-surface inclusions. Unlike uraninites in the basement, the ThO_2 contents of the uraninites in the supracrustal are either below detection limit or very low (maximum ThO_2 is ~0.4 wt%; Fig. 6a). The UO_2 and PbO contents of the grains vary from 73.90 to 88.66 wt% and 6.80 to 18.88 wt%, respectively (Fig. 6a and b). The highest concentration of Y_2O_3 is 1.13 wt% (Supplementary Appendixes A3). The ΣREY_2O_3 contents vary from 0.13 to 2.33 wt% (Fig. 6c), wherein most values are <2.0 wt% (Table 2 and Supplementary Appendix A3). The minor elements (Fig. 6d) in these uraninites have wide variation in concentration (SiO_2: bdl to maximum 10.61 wt%; CaO: bdl to 2.98 wt%; K_2O: 0.18–0.83 wt%). Iron is detected in most of the grains, wherein high FeO (up to 1.39 wt%) concentrations are predominantly found to be associated with tiny grains in proximity to magnetite, presumably indicating Fe excitation of magnetite hosting uraninite grains during analysis (cf. Pal and Rhede, 2013). The Al_2O_3 and Na_2O contents in uraninites are below detection limit excepting in few grains (Supplementary Appendix A3).

Unlike those from the basement, the different textural types of supracrustal uraninites are indistinguishable from each other in terms of their $\sum REY_2O_3$ content (Fig. 6c). The total minor element contents are also not very distinctive (Fig. 6d), excepting elevated contents of total minor elements, particularly of SiO_2 in few $U_{PB\text{-}3}$ grains (Fig. 6e). The minor element and PbO content of these grains and the associated coffinite, show strong negative correlation (Fig. 6d–f). Based on this observation, the supracrustal uraninites are classified into two groups, namely $PB_{G\text{-}1}$ and $PB_{G\text{-}2}$, characterized respectively by very low and elevated contents of minor elements respectively. Although both $U_{PB\text{-}1}$ and $U_{PB\text{-}2}$ uraninites belong to $PB_{G\text{-}1}$ compositional type, it is evident (Fig. 6b) that $U_{PB\text{-}1}$ uraninites contain higher PbO than the $U_{PB\text{-}2}$ uraninites. Thus $PB_{G\text{-}1}$ uraninites can further be sub-divided into two subgroups, namely $PB_{G\text{-}1a}$ and $PB_{G\text{-}1b}$, based on their PbO content. The $PB_{G\text{-}1a}$ and $PB_{G\text{-}1b}$ uraninites are characterized by high and low contents of PbO respectively.

To decipher the relation between $U_{PB\text{-}3}$ with U-silicates three representative grains, occurring along thin micro-cracks in quartz

and rimmed/replaced by coffinite, were investigated integrating BSE image, X-ray element maps (U, Pb, and Si; Fig. 6g–i) and EPM spot analysis. The grain in Fig. 6g, shows multiple zones in BSE image, wherein dark, pitted and patchy zones (close to the center and towards top right), extended or linked to the grain boundary, occur in an otherwise smoother, brighter uraninite. The X-ray maps display considerable depletion of Pb and enrichment of Si in the pitted areas (Fig. 6g; Table 1). Importantly the fresh and altered parts belong to compositional type $PB_{G\text{-}1a}$ and $PB_{G\text{-}2}$ respectively. Fig. 6h illustrates an association of phases in contact with muscovite and quartz, comprising rounded uraninite grains, likely to be remnants of partially resorbed earlier grains, which are surrounded by somewhat darker domains. X-ray maps demonstrate depletion of U and Pb and enrichment of Si in these domains compared to uraninite. High U and Si and low Pb content of some of these spots (#15 & #16) indicate that they are either partly coffinitized uraninite or coffinite formed from existing uraninite. Besides, the Pb-enriched phase towards the top and the dark phase in contact with coffinite (towards right in the BSE) respectively are galena and pyrite. The domain in Fig. 6i, demonstrates a similar association in which a euhedral uraninite is encircled by coffinite (in BSE). The interior of the uraninite appears to be pitted and partly replaced by coffinite as is evident from depletion in U and Pb (excepting the red spots in Pb-map, which are galena) and enrichment in Si (Fig. 6i and element distribution maps). The above textures and compositional characteristics of the chemically heterogeneous uraninite (Fig. 6g) suggest that the uraninites with $PB_{G\text{-}2}$ composition are likely the product of alteration of $PB_{G\text{-}1a}$ uraninite during an event of coffinitization/coffinite formation. Preservation of $PB_{G\text{-}1a}$ compositional types in these associations indicates that all $U_{PB\text{-}3}$ uraninites do not belong to $PB_{G\text{-}2}$ compositional type and therefore an individual textural type cannot always be specifically linked to a particular compositional type and vice versa. In the light of above discussion, we propose that the $PB_{G\text{-}1a}$ and $PB_{G\text{-}1b}$ represent the pristine compositions while the $PB_{G\text{-}2}$ represents the modified compositions.

6. Chemical age dating of uraninites

The EPMA U-Th-Pb_{Total} age determination of uraninite has been used by various workers in the last three decades (Kempe, 2003; Alexandre and Kyser, 2005; Cross et al., 2011; Pal and Rhede, 2013). This technique can be used on the fulfillment of two obligatory conditions. These are: (i) incorporation of no common Pb during mineral growth and (ii) no disturbances of the U, Th, and Pb systematics after crystallization of the mineral (Kempe, 2003). Uraninite satisfies the first criterion but many workers (Janeczek and Ewing, 1995; Kempe, 2003; Alexandre and Kyser, 2005; Deditius et al., 2007) have demonstrated that most natural uraninites are chemically heterogeneous at micron scale level, resulting analytical complications, if used for dating. Further, incompatibility of radiogenic Pb in the crystalline uraninite structure (Alexandre et al., 2015) and substitution of radiogenic Pb by other cations (e.g., Si, Ca, and Fe) during subsequent alteration (Alexandre and Kyser, 2005; Alexandre et al., 2015) may also affect chemical age. However, if trace and minor elements enter into uraninite mainly substituting radiogenic Pb, a meaningful age can be obtained by extrapolating the sum of the concentrations of minor (Si, Ca, K, Na, Al and Fe) and trace (REY) elements to zero, in age vs. concentration diagram, provided the pristine, unaltered uraninites did not contain significant trace and minor elements respectively (Alexandre and Kyser, 2005; Pal and Rhede, 2013).

Taking into account all necessary precautions, and considering all Pb to be radiogenic, we have first used the formulation of Montel et al. (1996) to determine the spot ages from the EPMA data. In general, the obtained uraninite ages from both the basement and the supracrustal rocks show wide ranges (Supplementary Appendices A2 and A3). However, as the uraninites are texturally and compositionally diverse and there are visible, textural and chemical evidence of alteration, the obtained ages need to be sorted and evaluated integrating textural and chemical features for a meaningful interpretation (e.g., Kempe, 2003). Ages obtained from grains or part of grains (unaltered parts in chemically heterogeneous grains), without any visible sign of alteration and having negligible concentration of total minors and/or REEs (represented by compositional types $MC_{G\text{-}1a}$, $MC_{G\text{-}1b}$, $PB_{G\text{-}1a}$ and $PB_{G\text{-}1b}$) are statistically evaluated to get the most probable age. For the spot ages obtained from grains, containing higher contents of trace/minor elements (compositional types $MC_{G\text{-}2}$ and $PB_{G\text{-}2}$) we have adopted the method of extrapolation (Alexandre and Kyser, 2005; Pal and Rhede, 2013) to obtain a meaningful age. Summary of different textural types, their compositional characters and ages is given in Table 1.

6.1. Basement

Spot ages obtained from the pristine uraninites ($MC_{G\text{-}1a}$ and $MC_{G\text{-}1b}$) in the basement range between 864 and 1896 Ma (Supplementary Appendix A2). The relative probability plots, constructed using Isoplot\Ex (Ver. 3.70; Ludwig, 2000), show two prominent probability peaks at ~0.96, and ~1.20 Ga, apart from a minor peak at ~1.88 Ga (Fig. 7a). Uraninites, belonging to $U_{MC\text{-}1}$ textural type and $MC_{G\text{-}1a}$ compositional type, consistently yield the intermediate age of ~1.20 Ga, excepting the altered grains which compositionally belong to $MC_{G\text{-}2}$. On the contrary, uraninites, belonging to $U_{MC\text{-}2}$ textural type and $MC_{G\text{-}1b}$ compositional type, yield the youngest age (~0.96 Ga).

Uraninites with $MC_{G\text{-}2}$ compositions and represented mainly by $U_{MC\text{-}3}$ textural types, display strong negative correlation between ΣREY_2O_3 contents and corresponding ages (Fig. 7b), which indicate significant control of trace elements in the modification of actual age. Strong negative correlation between $\sum REY_2O_3$ and PbO (Fig. 5c) further suggests that the ages were modified mainly due to the substitution of Pb by these elements. The role of $\sum REY_2O_3$ and PbO in the modification of ages is also evident from chemically heterogeneous grains (Fig. 5g), in which the intermediate age is obtained from the REE-poor, PbO-rich fresh zones (compositionally $MC_{G\text{-}1a}$) and lower and variable ages from the REE-rich, PbO-poor altered zones (compositionally $MC_{G\text{-}2}$). An age of ~1.22 Ga, similar to that of $U_{MC\text{-}1}/MC_{G\text{-}1a}$ uraninites, is obtained for the $U_{MC\text{-}3}/MC_{G\text{-}2}$ uraninites by extrapolating the $\sum REY_2O_3$ content to zero, using a best fit line on the age vs. $\sum REY_2O_3$ binary plot (Fig. 7b). The correlation between the concentrations of minor elements with the corresponding ages is very weak (Fig. 7c) and thus these elements had insignificant influence on the modification of actual age of the basement uraninite.

6.2. Supracrustals

The uraninite grains in quartzite yield spot ages varying from 616 to 1520 Ma (Supplementary Appendix A3). The ages obtained from the unaltered grains, having very low minor and trace element contents ($PB_{G\text{-}1a}$ and $PB_{G\text{-}1b}$) document a bimodal distribution, comprising one population at ~1.24 Ga and the other at ~1.01 Ga (Fig. 7d). The $U_{PB\text{-}1}$ uraninites having $PB_{G\text{-}1}$ compositions invariably belong to the older population (~1.24 Ga). In addition, $U_{PB\text{-}3}$ uraninites, retaining the $PB_{G\text{-}1a}$ compositions at places, also yield this older age (Fig. 6g–i; Table 2). On the contrary, $U_{PB\text{-}2}$ uraninites having $PB_{G\text{-}1b}$ composition belong to the younger population (~1.01 Ga).

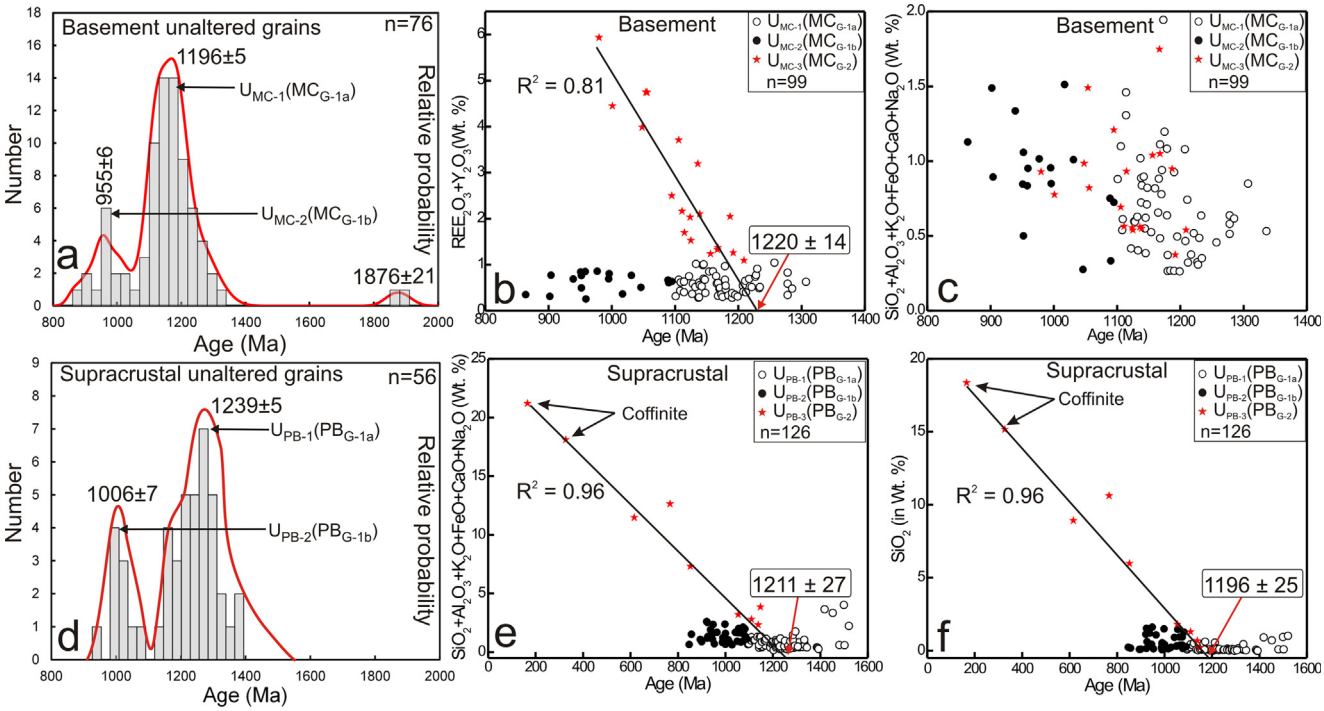

Fig. 7. (a) Relative probability plots and histograms showing statistically significant age peaks for the U_{MC-1} and U_{MC-2} uraninites that retain pristine compositions (MC_{G-1a} and MC_{G-1b} respectively) from the basement and define two distinct ages; (b) age vs. $\sum REY_2O_3$ plot of MC_{G-2} compositions, interpreted as modified product, show strong negative correlation defining an age of 1220 ± 14 at zero value of $\sum REY_2O_3$; (c) no correlation between age and total minor elements indicating insignificant control of minors on the ages; (d) relative probability plots and histograms showing statistically significant age peaks for the U_{PB-1} and U_{PB-2} uraninites retaining pristine compositions (PB_{G-1a} and PB_{G-1b} respectively) from the supracrustal define two distinct ages; (e) and (f) show strong correlations between age with total minors and SiO_2 of PB_{G-2} compositions, interpreted as modified products, defining ages of 1211 ± 27 Ma 1196 ± 25 Ma respectively at zero concentrations of total minors and SiO_2.

The PB_{G-2} uraninites, along with coffinite, show negative correlation between concentrations of total minor elements ($SiO_2 + Al_2O_3 + K_2O + FeO + CaO + Na_2O$) and calculated ages (Fig. 7e) implying influence of minor elements on the modification of ages. Further, the influence of SiO_2 is significantly higher as compared to the other minor elements (Fig. 7f). Negative correlation between minor elements and PbO (Fig. 6d–f) lends support to the fact that substitution of PbO by minor elements, particularly SiO_2, leading to coffinitization at places, was responsible for such modification. Such a mechanism is also evident from the compositionally heterogeneous U_{PB-3} grain (Fig. 6g), wherein the intermediate age is obtained from the minor element-poor, PbO-rich fresh zones (compositionally PB_{G-1a}) and lower and variable ages from the minor element-rich, PbO-poor altered zones (compositionally, PB_{G-2}). An age of ~1.21 Ga is obtained for the PB_{G-2} uraninites by extrapolating the total minor element contents ($SiO_2 + Al_2O_3 + K_2O + FeO + CaO + Na_2O$) to zero, using a best fit line in the age vs. minor elements binary plot (Fig. 7e). Unlike the modified uraninites in the basement, the ΣREY_2O_3 (Supplementary Appendix A3) contents of the modified uraninites in the supracrustal quartzite are low and do not show strong correlation either with age or PbO and therefore, the influence of the REEs on the ages is minimal.

7. Discussion

7.1. Geochemical and geochronological evolution of uranium mineralization

Uranium mineralization in the Samarkiya area is very low grade in nature and therefore uraninite, the main ore mineral of uranium, is scanty. Uraninite occurs as inclusion in different minerals and can be broadly classified into different textural types based on their shape, relative position in the host mineral and association of secondary minerals. However, there is no (a) distinct relation among the different textural types, (b) obvious difference in their modes of occurrence or (c) unique relation with the metamorphic/deformation fabric and metamorphic minerals. This hinders proposition of any meaningful paragentic sequence, based solely on proposed textural classification, which could be used to develop a model of geochemical and geochronological evolution of uranium mineralization. However, the different compositions and ages of diverse textural types of uraninites in tandem with intra-grain compositional and age variations collectively provide important clues to geochemical and geochronological evolution of uranium mineralization.

Uraninites from the basement show strong compositional variations defining three populations based on $\sum REY_2O_3$ and PbO content. The compositionally distinct uraninites define distinct age populations. The oldest age of ~1.88 Ga, obtained only from two grains, suggests either very minor contribution of this event in mineralization or the footprints of this event was obliterated during subsequent superimposed episodes. Barring the exception of these two uraninites, the unaltered, $\sum REY_2O_3$-poor pristine uraninites (MC_{G-1a} and MC_{G-1b}) define two distinct ages of ~1.20 Ga and ~0.96 Ga. The ~1.20 Ga age is represented by U_{MC-1} uraninites, occurring inside the host mineral, which are neither connected to the grain boundary through micro-crack nor replaced by secondary minerals (e.g., Fig. 3d and e). After being included, these grains were therefore likely shielded by the host mineral from subsequent fluid-assisted alteration, if any, and thus preserved the actual age. Based on the ubiquitous presence of uraninite defining this age, we propose that ~1.20 Ga event is the first major event (second after the 1.88 Ga event) of uranium mineralization in the basement. The youngest age of ~0.96 Ga is displayed by U_{MC-2}

euhedral uraninites that occur close to the grain boundary of the host mineral (e.g., Fig. 3f). These uraninites may represent neo-mineralization through fresh influx of uranium or neo-crystallization of remobilized uranium from existing uraninite. Although the studied uraninites occur at the grain boundary, they are included in the host minerals and their compositions are otherwise indistinguishable from the ~1.20 Ga uraninites excepting the PbO contents. Therefore, a fluid-mediated recrystallization or pervasive alteration of existing ~1.20 Ga uraninite resulting in complete Pb loss and resetting of isotopic clock at ~0.96 Ga remains a strong possibility. Migration of fluids along the grain boundary likely facilitated the process.

The compositionally distinct REY-rich uraninites commonly occur in association with REE-phases and at the first instance may appear to be the product of new event of mineralization (e.g., Fig. 3g). However, strong negative correlation between PbO and ΣREY_2O_3 (Fig. 5c), indicate that high REY-content is not the product of primary crystallization rather reflects later substitution of radiogenic Pb by $\sum$REY. This proposition is further substantiated by the partial replacement of low-REY, high-PbO uraninite (belonging to MC_{G-1a}) by this high-REY, variable PbO uraninite (MC_{G-2}). Moreover, the best fit line in $\sum REY_2O_3$ vs. age yields an age (~1.22 Ga) very similar to that of the pristine ~1.20 Ga uraninite at zero value of $\sum REY_2O_3$ further supporting derivation of REY-rich uraninites from the ~1.20 Ga uraninites. The associated micro-cracks likely acted as the fluid conduit. It is recalled that post-uraninite hydrothermal alteration is evident from alteration halos in plagioclase surrounding uraninite inclusions and from other mineral-alterations. The source of REEs is uncertain. From the association of partially resorbed patchy monazite with REY- and Th-rich uraninite (Fig. 3g) we infer monazite to be one of the possible sources of Th + REY. Previously, Alexandre et al. (2015) have suggested that monazite can act as a potential local source of Th for uraninite. We have described that the alteration halos in plagioclase at places contain REE-bearing unknown phases. Therefore, REEs may be freshly introduced or redistributed during the alteration, which formed the REY-rich uraninite. This may be the case where REE-minerals replace the existing uraninite resulting in REY-enrichment of the latter. We cannot confirm the age of this alteration event. However, as this event modified the ~1.2 Ga, REY-poor MC_{G-1a} uraninites only (evident from texture and convergence of ages obtained from probability histogram of unaltered grains and best fit line of altered grains) it stands to reason that this event took place sometime between 1.20 and 0.96 Ga.

Similar to those in the basement, uraninites in the supracrustal rocks are also compositionally diverse and define three compositional types based on total content of minor elements and PbO. Most uraninites, however, are poor in minor and trace elements excepting a few that contain elevated contents of minor elements. The unaltered, pristine, U_{PB-1} uraninites occurring within quartz and magnetite, define the highest age of ~1.24 Ga. As these grains were perhaps not affected by later hydrothermal event, we propose that the major event of uranium mineralization in the supracrustal rocks took place at ~1.24 Ga. Euhedral uraninite belonging to U_{PB-2} textural types, commonly associated with micro-cracks, yield the younger age of ~1.01 Ga. These uraninites may represent in situ precipitation from a new influx of U-rich fluid (hence neo-mineralization) or remobilized uranium from earlier uraninites. However, as these uraninites are compositionally indistinguishable from ~1.24 Ga uraninites (U_{PB-1}) except having lower PbO content, they may be the product of fluid-mediated recrystallization or pervasive alteration of existing ~1.24 Ga, U_{PB-1} uraninites, which resulted in complete Pb loss and resetting of isotopic clock at ~1.01 Ga. Although few data are available, a strong negative relationship between SiO_2 + CaO and PbO (Fig. 6f) of the minor element-rich uraninites and associated coffinite suggest the derivation of this uraninite composition through substitution of radiogenic Pb by minor elements during the process of coffinitization. The chemical texture of large uraninite, wherein the unaltered and altered parts represent the low-minor, high PbO and high-minor, variable PbO uraninite respectively, is unambiguous evidence of formation of the latter from the former. This is also supported by the age, obtained by extrapolating the total minor element concentrations to zero in total minor elements vs. age plot, similar to that of the ~1.24 Ga, PB_{G-1a} uraninites. This alteration event is presumably linked to the process of silicification, the brecciated and silicified quartzite was subjected to. Besides, formation of galena is perhaps due to redistribution/removal of radiogenic Pb during sulfidation, assisted by extensive fracturing during replacement of uraninite. Presence of pyrite in such association lends support to such sulfidation event. This explains why the uraninites of such association are occasionally characterized by low and variable PbO contents and therefore the obtained spot ages cannot be directly used in probability diagram.

On the basis of the elemental distributions within the pristine and modified uraninite grains, it is proposed that the compositional variations of uraninites in the Samarkiya deposit is controlled by both original compositional variations during crystallization and subsequent incorporation and expulsion of elements during superimposed hydrothermal alteration. Thus, the uraninites demonstrate diverse events of uranium mineralization/-mobilization and modification of earlier uraninite compositions by later superimposed hydrothermal episodes (e.g., Pal and Rhede, 2013; Macmillan et al., 2016).

7.2. Nature of uranium mineralization

Our study demonstrates substantial substitution of different trace and minor elements (Th, REY, Ca, Si, Fe, and K) into the structure of uraninite. By virtue of similar ionic radii and similar charges (which can be balanced easily through one-to-one or coupled substitution) of Th^{4+} (1.05 Å), REE^{3+} (0.98–1.16 Å), and Y^{3+} (1.02 Å) as that of U^{4+} (1.00 Å), uraninite can accommodate these elements (Shannon, 1976) during its formation. Moreover, previous workers have also reported late incorporation of elements (viz., REY, Si, Ca, K, and Na) into the uraninite structure during later events (Kempe, 2003; Alexandre and Kyser, 2005; Pal and Rhede, 2013; Alexandre et al., 2015; Macmillan et al., 2016). Incorporation of elements into the structure of uraninite is essentially a function of temperature and element availability. The incorporation of Th^{+4} into the structure of uraninite is also influenced by the processes related to enrichment of uranium in the fluid or melt that precipitates uraninite (Alexandre et al., 2015). For example, in intrusive and high temperature metasomatic deposits, initial enrichment of uranium as U^{+4} results during partial melting of the parent rock, fractional crystallization of the melt and exsolution of a magmatic-hydrothermal fluid due to incompatible behavior of U^{+4} (Cuney and Kyser, 2009). The same is also true for Th^{+4} as it is readily soluble and behaves similarly at high temperature magmatic environment (Mercadier et al., 2011; Depiné et al., 2013; Cuney, 2010; Frimmel et al., 2014). Therefore, Th^{+4} is available in the vicinity and is easily "camouflaged" at the site of U^{+4} in uraninite structure during crystallization (Alexandre et al., 2015). On the contrary, in cases where U mobilizes in the form of U^{+6} under oxidizing condition that prevails in most low temperature, surface-derived diagenetic or hydrothermal fluid, Th^{+4} is insoluble and therefore is decoupled from uranium (Takeno, 2005). Consequently, uraninite precipitated by reduction of U^{+6} to U^{+4} (e.g., in sandstone-hosted deposits), from such a fluid, are depleted in Th^{+4} (Alexandre et al., 2015). At higher temperatures, the uraninite structure permits substantial incorporation of trace elements such as REE_2O_3 and Y_2O_3, apart from negligible amount of minor elements (e.g.,

SiO_2 and CaO), while at lower temperature minor elements are more easily substituted than REEs in uraninite (Alexandre and Kyser, 2005; Bastrakov et al., 2010; Mercadier et al., 2011; Depiné et al., 2013; Frimmel et al., 2014; Macmillan et al., 2016). The fractionation of REE_2O_3 into uraninite strikingly increases with the crystallization temperature (Eglinger et al., 2013). From the foregoing discussion, it stands to reason that the concentrations of different elements and the UO_2/ThO_2 ratio can be used as proxies to decipher the origin of uraninite and for semi-quantitative estimation of temperature of uraninite formation (Fryer and Taylor, 1987; Mercadier et al., 2011; Frimmel et al., 2014; Mukhopadhyay et al., 2016). However, we emphasize that in a deposit, which was subjected to post-mineralization hydrothermal fluid influx resulting in compositional modification of existing uraninite, it is mandatory to distinguish between original and modified concentrations of the proxy-elements for any meaningful interpretation of composition.

The ca. 1.88 Ga ages were obtained only from two grains in the basement. Although these grains contain elevated ThO_2 and $\sum REY_2O_3$, we neither found intra-grain compositional heterogeneity nor we could use element correlation plots to examine whether these elements are pristine or introduced during subsequent processes. Therefore, we cannot comment on their possible origin based on the concentrations of these elements. All the ~1.20 Ga and ~0.96 Ga uraninites ($U_{MC\text{-}1}$ and $U_{MC\text{-}2}$ belonging to $MC_{G\text{-}1a}$ and $MC_{G\text{-}1b}$ compositions respectively) along with the modified grains ($MC_{G\text{-}2}$ compositions) having high REY-content are characterized by high absolute concentrations of ThO_2 (Supplementary Appendix A2). This indicates their derivation from high temperature, such as magmatic, magmatic-hydrothermal and metamorphic process (e.g., Grandstaff, 1981; Frimmel et al., 2014; Alexandre et al., 2015). Strong negative correlation between UO_2 and ThO_2 (Fig. 5a) in combination with the hyperbolic trend defined by UO_2/ThO_2 vs. ThO_2 (Fig. 5f), suggest primary incorporation of ThO_2 into the uraninite structure, during crystallization from a high temperature fluid (Grandstaff, 1981; Mukhopadhyay et al., 2016). Additionally, this inference is further substantiated from the U/Th vs. ∑REE binary diagram, wherein these pristine grains typically plot within the high temperature (>450 °C; Fig. 8) magmatic/metamorphic field. We have demonstrated that the high $\sum REY_2O_3$ contents of the modified uraninites are not primary and were incorporated during hydrothermal alteration. Therefore, high REY contents of these uraninites cannot and should not alone be used to decipher their origin, although this suggests a high temperature alteration of $MC_{G\text{-}1a}$ uraninites.

Unlike the uraninites in the basement, none of the uraninites in the supracrustal contain significant ThO_2 or $\sum REY_2O_3$. It therefore stands to reason that both the ~1.24 Ga and ~1.0 Ga uraninites formed either at a much lower temperature compared to the basement uraninites or resulted from decoupling of Th from U during their transport from the source to the depositional site by an oxidized fluid. Besides, some of the modified uraninites in the supracrustal contain high and variable concentrations of minor elements, but low $\sum REY_2O_3$ unlike the modified uraninites in the basement. Primary incorporation of Ca into the uraninite structure is possible, due to the close similarity between the ionic radii of Ca^{+2} and U^{+4} (Frimmel et al., 2014). However, the invariable increase of Ca along with SiO_2 (Fig. 6e and f) and higher concentrations of these elements in the modified parts of uraninite collectively support later incorporation of CaO into the structure of uraninite during a low temperature alteration. The proposition of low temperature formation and subsequent low temperature alteration of uraninite is further supported by distinct clustering of supracrustal uraninites (those with detectable amount of ThO_2) within low temperature (<350 °C) to slightly high temperature (>450 °C) field (i.e., away from the basement uraninites) in the U/Th vs. ∑REE binary diagram (Fig. 8).

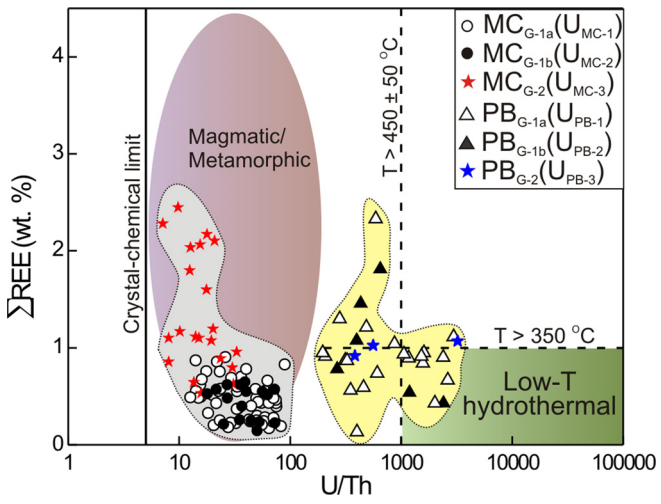

Fig. 8. U/Th vs. total ∑REE plot (in wt%) for uraninite grains from the basement and the supracrustal (after Mercadier et al., 2011; Frimmel et al., 2014). Note that the uraninites from the basement are likely related to high temperature, magmatic/magmatic-hydrothermal/metamorphic process, whereas those from the supracrustal crystallized from a low to moderate temperature fluid.

7.3. Uranium mineralization in the context of known geological events

The oldest Paleoproterozoic 1876 ± 21 Ga age, even though constrained only by two uraninite analyses, overlaps with the age (~1.82 Ga) estimated for one of the phases of metamorphism in the central part of the ADFB (Buick et al., 2010; Ozha et al., 2016a). Further, recently, Kaur et al. (2017), reported granitic magmatism at ca. ~1.86–1.81 Ga from the northern part of the ADFB (i.e., Khetri area; Fig. 1b). Thus, the ~1.88 Ga age, obtained from the basement uraninite can be related to the pervasive tectono-metamorphic-magmatic event in the ADFB, and represents the first stage of U mineralization in the MC rocks. Derivation from a high temperature magmatic, magmatic-hydrothermal or metamorphic process can suitably explain the high Th and REY content of this earliest recognized uraninite in the basement.

The ubiquitous presence of uraninites yielding ~1.20 and ~1.24 Ga ages in the basement and the supracrustals respectively suggest a major mineralization during ~1.24–1.20 Ga in Samarkiya area. Distinct compositional differences between uraninites in the basement and in the supracrustals are suggestive of different processes or fluid involved in this mineralization. It is uncertain whether the ~1.20 Ga and ~1.24 Ga ages obtained from uraninite in the basement and the supracrustal respectively represent two discrete events. However, uraninite ages obtained from probability diagram and best fit line are collectively indistinguishable between the basement and the supracrustal. It is thus highly probable that uraninites of these ages are the product of same geological event. From the Samarkiya and surrounding areas, Ozha et al. (2016a) have reported ~1.37–1.35 Ga ages both within the MC and the PB rocks that represent the age of an amphibolite facies metamorphic event (M_2). Recently, Hazarika et al. (in press) reported a hydrothermal event at ~1.28–1.27 Ga postdating this peak metamorphic event from the MC rocks of the Samarkiya area. Hence, in the light of the available age data, it is reasonable to infer that the age (~1.24–1.20 Ga) obtained from the basement and the supracrustal rocks represent a post-peak metamorphic (M_2 event of Ozha et al., 2016a) retrograde or hydrothermal event of neo-m ineralization/remobilization. Presence of uraninite as inclusions in the host metamorphic minerals suggests that uraninite crystal-

lized either prior to or along with the host minerals. Moreover, as the uraninite alteration took place sometime between ~1.20–0.96 Ga and there is definite control of relative position of uraninite in the host on the extent of uraninite alteration, the process of uraninite incorporation in the host mineral must have taken place prior to the formation of last stage uraninite. It is possible that these uraninites crystallized during or incorporated in the host mineral during a new metamorphic event following the ~1.37–1.35 Ga but prior to the ~1.0 Ga event. There is no robust and well-construed data on such an event from the study area. McKenzie et al. (2013) reported abundant detrital zircon of ~1.20 Ga from the Alwar Group of the Delhi Supergroup. It is possible that a metamorphic event at ~1.20 Ga was responsible for uranium mineralization or incorporation of uraninite in the host metamorphic minerals. More studies are warranted in this direction.

The youngest ages ~0.96 and ~1.01 Ga obtained from the basement and the supracrustal rocks respectively, is the last event of uraninite formation in the Samarkiya area. The textures and compositions of uraninites representing this age collectively suggest that this event may represent in situ recrystallization, alteration of existing uraninite or formation of new uraninite from fresh influx of uranium. Similar ages (~1.0 Ga) were widely reported from different parts of the ADFB (Buick et al., 2006, 2010; Bhowmik et al., 2010; Ozha et al., 2016a; Hazarika et al., in press) (Fig. 1a and b), which represent the onset of the Grenvillian orogeny in the belt and thereby formation of the Rodinian crust. Further, recently, Yadav et al. (2016) have reported near similar U-Pb (concordant) and Pb-Pb (isochron) age of davidite (0.93–0.90 Ga) associated with uraninite and brannerite from the Bhicun area (Fig. 1b), which they infer to be the age of the U mineralization in the area. These authors have further linked the mineralization age with the tectono-thermal event related to the Grenvillian orogeny. Consequentially, we infer the last event of U mineralization/mobilization in the area to be related to this major tectono-thermal event and formation of the Rodinia supercontinent. Further, the Neoproterozoic age (~1.01–0.96 Ga) of the present study validates the extension of the proposed Grenvillian front (by Bhowmik et al., 2010) towards further east as previously suggested by Ozha et al. (2016a).

8. Conclusions

In the Samarkiya area, central Rajasthan, uranium mineralization is hosted by deformed and metamorphosed rocks, in which uraninite occurs as disseminated inclusions in various major rock forming minerals. Uraninites do not have any compelling textural and morphological character or distinctive association with metamorphic minerals and structural fabric, which can be used to develop a convincing paragenetic sequence or can be linked to the tectono-metamorphic evolution of the host rock. However, in this study we demonstrate that meaningful model of origin, and geochemical-temporal evolution of uranium mineralization in such cases can be developed integrating texture, geochemistry, and spot age determinations including intra-grain compositional and age variations. The present study deduces three stages of uranium mineralization/mobilization (at ~1.88, ~1.24–1.20, ~1.01–0.96 Ga). The oldest age of ~1.88 Ga, obtained from uraninite in the basement, represents the first stage of mineralization. Similar mineralization age has been reported from uraninite and allanite in the Proterozoic Singhbhum Shear Zone, eastern India (Pal et al., 2011; Pal and Rhede, 2013) and is considered to be the earliest recorded event of uranium mineralization in that shear zone. It therefore stands to reason that such an event of uranium mineralization may be linked to the overall Proterozoic crustal evolution in the Indian subcontinent, although the details are yet to be unraveled. A large number of uraninites, both from the basement and the supracrustal, preserve an age of ~1.24–1.20 Ga, which we interpret to be the major and pervasive event of uranium mineralization in the Samarkiya area. We suggest that more rigorous studies on the geochronology of metamorphic and igneous rocks are required for detailed understanding of the tectono-thermal evolution vis-à-vis mineralization during this period. Subsequently, the mineralized rocks were subjected to fluid-induced alteration which eventually modified/altered the compositions of pristine uraninites. Retention of compositions and ages of older uraninite even in partially altered single grains indicate that the alteration process was not pervasive enough to obliterate the earlier geochemical footprints in large grains and therefore provides invaluable archives of previous events. The REY-enrichment in the basement uraninite and Si (-Ca) enrichment in the supracrustal uraninite perhaps suggest redistribution of these elements in the respective host rock and not addition from extraneous sources. Later, during Neoproterozoic (~1.01–0.96 Ga), either some of existing uraninites were altered leading to complete Pb-loss, or new uraninite crystallized/re-crystallized as a consequence of fresh hydrothermal event, which is inferred to be the third and the youngest hydrothermal event in the area. Thus, the Samarkiya area witnessed multiple metamorphic/hydrothermal events resulting in uraninite precipitation, alteration and recrystallization, the footprints of which are preserved in uraninite. Further, the three discrete episodes spanning ~0.92 Ga represents growth of different generation of uraninite where the last one pertains to formation of Rodinia. Thus, our study demonstrates the potential of uraninite geochemistry and dating in archiving the timings of various primary mineralization and associated later alteration events as well as in deciphering their probable origin.

Acknowledgments

This research work was funded by the Board of Research in Nuclear Sciences (BRNS), India, Project No. 2011/36/33-BRNS to BM. MKO thanks BRNS and IIT Kharagpur for financial assistance in the form of a research fellowship. This work forms a part of the doctoral thesis of MKO. SEM-BSE imaging and EPMA data were generated by equipment procured through a DST funding (IR/S4/ESF-08/2005) to the Department of Geology and Geophysics, IIT Kharagpur. The authors acknowledge stimulating discussions with D. Upadhyay and K. L. Pruseth. G. S. Yadav, S. K. Varghese, and S. Barman of the Atomic Minerals Directorate for Exploration and Research (AMDER) are thanked for their help during fieldwork. Pranjit Hazarika and Saptarshi Sinha helped in EPM analysis. Constructive criticism, comments and suggestions by Gema R. Olivo and one anonymous reviewer, along with editorial suggestions by Franco Pirajno helped improving the manuscript significantly and are gratefully acknowledged.

Appendix A. Supplementary data

Supplementary data associated with this article can be found, in the online version, at http://dx.doi.org/10.1016/j.oregeorev.2017.04.010.

References

Alexandre, P., Kyser, T.K., 2005. Effects of cationic substitutions and alteration in uraninite, and implications for the dating of uranium deposits. Can. Mineral. 43, 1005–1017.

Alexandre, P., Kyser, K., Layton-Matthews, D., Joy, B., Uvarova, Y., 2015. Chemical compositions of natural uraninite. Can. Mineral. 53, 595–622.

Bastrakov, E.N., Jaireth, S., Mernagh, T.P., 2010. Solubility of uranium in hydrothermal fluids at 25°–300°: implications for the formation of uranium deposits. Geosci. Austral. Rec. 29.
Bhowmik, S.K., Bernhardt, H.J., Dasgupta, S., 2010. Grenvillian age high-pressure upper amphibolite-granulite metamorphism in the Aravalli-Delhi mobile belt, Northwestern India: new evidence from monazite chemical age and its implication. Precambrian Res. 78, 168–184.
Biju-Sekhar, S., Yokoyama, K., Pandit, M.K., Okudaira, T., Yoshida, M., Santosh, M., 2003. Late Paleoproterozoic magmatism in Delhi Fold Belt, NW India and its implication: evidence from EPMA chemical ages of zircons. J. Asian Earth Sci. 22, 189–207.
Bonhoure, J., 2007. Géochimie des éléments de terresrareset du plombdans les oxydesd'uraniumnaturels. Dissertation, Vandoeuvre-les-Nancy (INPL).
Buick, I.S., Allen, C., Pandit, M., Rubatto, D., Hermann, J., 2006. The Proterozoic magmatic and metamorphic history of the Banded Gneiss Complex, central Rajasthan, India: LA-ICP-MS U-Pb zircon constraints. Precambrian Res. 151, 119–142.
Buick, I.S., Clark, C., Rubatto, D., Hermann, J., Pandit, M.K., Hand, M., 2010. Constraints on the Proterozoic evolution of the Aravalli-Delhi Orogenic belt (NW India) from monazite geochronology and mineral trace element geochemistry. Lithos 120, 511–528.
Choudhary, A.K., Gopalan, K., Anjaneya Sastry, C., 1984. Present status of the geochronology of the Precambrian rocks of Rajasthan. Tectonophysics 105, 131–140.
Cross, A., Jaireth, S., Rapp, R., Armstrong, R., 2011. Reconnaissance-style EPMA chemical U-Th–Pb dating of uraninite. Aust. J. Earth Sci. 58, 675–683.
Cuney, M., Kyser, K., 2009. Recent and not-so-recent developments in uranium deposits and implications for exploration. Min. Assoc. Canada 39, 215.
Cuney, M., 2010. Evolution of uranium fractionation processes through time: driving the secular variation of uranium deposit types. Econ. Geol. 105, 553–569.
Dahlkamp, F.J., 1993. Uranium Ore Deposits. Springer-Verlag, Berlin.
Deb, M., Pal, T., 2015. Mineral potential of Proterozoic intracratonic basins in India. Mem. Geol. Soc. London 43, 309–325.
Deb, M., Thorpe, R.I., Kristic, D., Corfu, F., Davis, D.W., 2001. Zircon U-Pb and galena Pb isotope evidence for an approximate 1.0 Ga terrane constituting the western margin of the Aravalli-Delhi orogenic belt, northwestern India. Precambrian Res. 108, 195–213.
Deditius, A.P., Utsunomiya, S., Ewing, R.C., 2007. Fate of trace elements during alteration of uraninite in a hydrothermal vein-type U-deposit from Marshall Pass, Colorado. USA. Geochim. Cosmochim. Acta 71, 4954–4973.
Depiné, M., Frimmel, H.E., Emsbo, P., Koenig, A.E., Kern, M., 2013. Trace element distribution in uraninite from Mesoarchaean Witwatersrand conglomerates (South Africa) supports placer model and magmatogenic source. Miner. Deposita 48, 423–435.
Eglinger, A., André-Mayer, A.S., Vanderhaeghe, O., Mercadier, J., Cuney, M., Decrée, S., Milesi, J.P., 2013. Geochemical signatures of uranium oxides in the Lufilian belt: from unconformity-related to syn-metamorphic uranium deposits during the Pan-African orogenic cycle. Ore Geol. Rev. 54, 197–213.
Finch, R.J., Murakami, T., 1999. Systematics and paragenesis of uranium minerals. Rev. Mineral. 38, 91–180.
Frimmel, H.E., Schedel, S., Brätz, H., 2014. Uraninite chemistry as forensic tool for provenance analysis. Appl. Geochem. 48, 104–121.
Fryer, B.J., Taylor, R.P., 1987. Rare-earth element distributions in uraninites: implications for ore genesis. Chem. Geol. 63, 101–108.
Grandstaff, D.E., 1976. A kinetic study of the dissolution of uraninite. Econ. Geol. 71, 1493–1506.
Grandstaff, D.E., 1981. Microprobe analyses of uranium and thorium in uraninite from the Witwatersrand, South Africa, and Blind River, Ontario, Canada. In: Armstrong, F.C. (Ed.), Genesis of Uranium- and Gold-Bearing Precambrian Quartz-Pebble Conglomerates. U.S. Geol. Surv, pp. J1–J5. Professional Paper.
Gopalan, K., Macdougall, J.D., Roy, A.B., Murali, A.V., 1990. Sm-Nd evidence for 3.3 Ga old rock in Rajasthan, north-western India. Precambrian Res. 48, 287–297.
Guha, D.B., Bhattacharya, A.K., 1995. Metamorphic evolution and high-grade reworking of the Sandmata Complex granulites. In: Continental Crust of Northwestern and Central India. In: Gupta, K.R., Sinha-Roy, S. (Eds.), . Mem. Geol. Surv. India, vol. 31, pp. 163–198.
Gupta, B.C., 1934. The geology of central Mewar. Mem. Geol. Surv. India 65, 107–168.
Gupta, S.N., Arora, Y.K., Mathur, R.K., Iqbaluddin, Prasad, B., Sahai, T.N., Sharma, S.B., 1997. The Precambrian geology of the Aravalli region, southern Rajasthan and north-eastern Gujarat. Mem. Geol. Surv. India 123, 1–262.
Hazarika, P., Upadhyay, D., Mishra, B., 2013. Contrasting geochronological evolution of the Rajpura-Dariba and Rampura-Agucha metamorphosed Zn-Pb deposit, Aravalli-Delhi Belt. India. J. Asian Earth Sci. 73, 329–339.
Hazarika, P., Mishra, B., Ozha, M.K., Pruseth, K.L., 2017. An improved EPMA analytical protocol for U-Th-Pbtotal dating in xenotime: Age constrains from polygenetic Mangalwar Complex, Northwestern India. Chemie der Erde 77, 69–79. http://dx.doi.org/10.1016/j.chemer.2017.01.010.
Heron, A.M., 1953. The Geology of Central Rajputana. Mem. Geol. Surv. India 79, 1–339.
IAEA 2016. Uranium-2016: Resources, Production and Demand. A joint report by Nuclear Energy Agency and the International Atomic Energy Agency.
Janeczek, J., Ewing, R.C., 1992. Structural formula of uraninite. J. Nucl. Mater. 190, 128–132.
Janeczek, J., Ewing, R.C., 1995. Mechanisms of lead release from uraninite in the natural fission reactors in Gabon. Geochim. Cosmochim. Acta 59, 1917–1931.
Jefferson, C.W., Thomas, D.J., Gandhi, S.S., Ramaekers, P., Delaney, G., Brisbin, D., Cutts, C., Portella, P., Olson, R.A., 2007. Unconformity-associated uranium deposits of the Athabasca Basin, Saskatchewan and Alberta. Bulletin-Geol. Surv. Canada 588, 23.
Jercinovic, M.J., Williams, M.L., 2005. Analytical perils (and progress) in electron microprobe trace element analysis applied to geochronology: back-ground acquisition, interferences, and beam irradiation effects. Am. Mineral. 90, 526–546.
Kaur, P., Zeh, A., Chaudhri, N., 2017. Palaeoproterozoic (1.85 Ga) continental arc magmatism, and Neoproterozoic (0.87 Ga) metamorphism in the Aravalli-Delhi orogenic belt, NW India: New constraints from in situ zircon U-Pb-Hf isotope systematics, monazite dating and whole-rock (isotope) geochemistry. J. Asian Earth Sci. 136, 68–88.
Kempe, U., 2003. Precise electron microprobe age determination in altered uraninite: consequences on the intrusion age and the metallogenic significance of the Kirchberg granite (Erzgebirge, Germany). Contrib. Mineral. Petrol. 145, 107–118.
Kotzer, T.G., Kyser, T.K., 1993. O, U, and Pb isotopic and chemical variations in uraninite: implications for determining the temporal and fluid history of ancient terrains. Am. Mineral. 78, 1262–1274.
Kyser, K., Hiatt, E., Renac, C., Durocher, K., Holk, G., Deckart, K., 2000. Diagenetic fluids in Paleo- and Meso-Proterozoic sedimentary basins and their implications for long protracted fluid histories. In: Kyser, Kyser, T.K. (Eds.), Fluids and Basin Evolution. Mineralogical Association of Canada Short Course Series, 28, pp. 225–226.
Ludwig, K.R. 2000. User's manual for Isoplot/ex rev. 2.49: A geochronological Toolkit for Microsoft Excel: Berkeley Geochronology Center, Spec. Publication 1a, 1–56.
Macmillan, E., Cook, N.J., Ehrig, K., Ciobanu, C.L., Pring, A., 2016. Uraninite from the Olympic Dam IOCG-U-Ag deposit: linking textural and compositional variation to temporal evolution. Am. Mineral. 101, 1295–1320.
McKenzie, N.R., Hughes, N.C., Myrow, P.M., Banerjee, D.M., Deb, M., Planavsky, N.J., 2013. New age constraints for the Proterozoic Aravalli-Delhi successions of India and their implications. Precambrian Res 238, 120–128.
Mercadier, J., Cuney, M., Lach, P., Boiron, M.C., Bonhoure, J., Richard, A., Kister, P., 2011. Origin of uranium deposits revealed by their rare earth element signature. Terra Nova 23, 264–269.
Mercadier, J., Annesley, I.R., McKechnie, C.L., Bogdan, T.S., Creighton, S., 2013. Magmatic and metamorphic uraninite mineralization in the Western Margin of the trans-hudson orogen (Saskatchewan, Canada): a uranium source for unconformity-related uranium deposits? Econ. Geol. 108, 1037–1065.
Montel, J.M., Foret, S., Veschambre, M., Nicollet, C., Provost, A., 1996. Electron microprobe dating of monazite. Chem. Geol. 131, 37–53.
Mukhopadhyay, J., Mishra, B., Chakrabarti, K., De, S., Ghosh, G., 2016. Uraniferous Paleoplacers of the Mesoarchean Mahagiri Quartzite, Singhbhum Craton, India: depositional controls, nature and source of >3.0 Ga Detrital Uraninites. Ore Geol. Rev. 72, 1290–1306.
Ozha, M.K., Mishra, B., Hazarika, P., Jeyagopal, A.V., Yadav, G.S., 2016a. EPMA monazite geochronology of the basement and supracrustal rocks within the Pur-Banera basin, Rajasthan: evidence of Columbia breakup in Northwestern India. J. Asian Earth Sci. 117, 284–303.
Ozha, M.K., Mishra, B., Jeyagopal, A.V., 2016b. Reaction aureoles around uraninites within biotite and plagioclase: evidence of low temperature sequential fluid alteration and LREE-mobilization from monazite. Mineral. Mag. 80, 556–584.
Pal, D.C., Rhede, D., 2013. Geochemistry and chemical dating of uraninite in the Jaduguda uranium deposit, Singhbhum Shear Zone, India—implications for uranium mineralization and geochemical evolution of uraninite. Econ. Geol. 108, 1499–1515.
Pal, D.C., Chaudhuri, T., McFarlane, C., Mukherjee, A., Sarangi, A.K., 2011. Mineral chemistry and in situ dating of allanite, and geochemistry of its host rocks in the Bagjata Uranium Mine, Singhbhum Shear Zone, India—implications for the chemical evolution of REE mineralization and mobilization. Econ. Geol. 106, 1155–1171.
Pandit, M.K., Carter, L.M., Ashwal, L.D., Tucker, R.D., Torsvik, T.H., Jamtveit, B., Bhusan, S.K., 2003. Age petrogenesis and significance of 1 Ga granitoids and related rocks from the Sendra area, Aravalli craton. NW India. J. Asian Earth Sci. 22, 363–381.
Pant, N.C., Kundu, A., Joshi, S., 2008. Age of metamorphism of Delhi Supergroup-rocks electron microprobe ages from Mahendragarh district. Haryana. J. Geol. Soc. India 72, 365–372.
Raja Rao, C.S., 1976. Precambrian sequences of Rajasthan. Miscellaneous Publication. Geol. Surv. India 23, 497–516.
Rao, N.C., Anand, M., Dongre, A., Osborne, I., 2010. Carbonate xenoliths hosted by the Mesoproterozoic Siddanpalli Kimberlite Cluster (Eastern Dharwar craton): implications for the geodynamic evolution of southern India and its diamond and uranium metallogenesis. Int. J. Earth Sci. 99, 1791–1804.
Ray, S.K., 1990. The albitite line of northern Rajasthan-A fossil intracontinental rift zone. J. Geol. Soc. India 36, 413–423.
Roy, A.B., Kröner, A., 1996. Single zircon evaporation ages constraining the growth of the Archaean Aravalli craton, northwestern Indian shield. Geol. Mag. 133, 333–342.
Roy, A.B., Kröner, A., Rathore, S., Laul, V., Purohit, R., 2012. Tectono-Metamorphic and Geochronologic Studies from Sandmata Complex, Northwest Indian Shield: Implications on Exhumation of Late-Palaeoproterozoic Granulites in an

Archaean-early Palaeoproterozoic Granite-Gneiss Terrane. J. Geol. Soc. India 79, 323–334.
Sarkar, G., Barman, T., Corfu, F., 1989. Timing of continental arc magmatism in northwest India: evidence from U-Pb Zircon geochronology. J. Geol. 97, 607–612.
Shaji, T.S., Desapati, T., Fahmi, S., Yadav, G.S., Pande, A.K., 2007. Occurrence of uraninite and brannerite in the Samarkiya area, Bhilwara district. Rajasthan. Curr. Sci. 92, 592–594.
Shannon, R.T., 1976. Revised effective ionic radii and systematic studies of interatomic distances in halides and chalcogenides. Acta Crystallogr. A. 32, 751–767.
Singh, Y., Viswanathan, R., Parihar, P.S., Maithani, P.B., 2013. X-ray crystallography of uraninites associated with the albitite belt of western India: Evidence for the high-temperature origin of uranium and associated mineralization. J. Geol. Soc. India. 81, 79–90.
Sinha-Roy, S., Malhotra, G., Mohanty, M., 1998. Geology of Rajasthan. Geol. Soc. India, Bangalore, 278p.
Suzuki, K., Kato, T., 2008. CHIME dating of monazite, xenotime, zircon and polycrase: protocol, pitfalls and chemical criterion of possibly discordant age data. Gondwana Res. 14, 569–586.
Takeno, N., 2005. Atlas of Eh-pH diagrams, inter comparison of thermodynamic databases. Geol. Surv. Japan, 419p.
Tobisch, O.T., Collerson, K.D., Bhattacharya, T., Mukhopadhyay, D., 1994. Structural relationship and Sm-Nd isotopic systematics of polymetamorphic granite gneisses and granitic rocks from central Rajasthan: implications for the evolution of Aravalli craton. Precambrian Res. 65, 319–339.
Volpe, A.M., Macdaugall, J.D., 1990. Geochemistry and isotopic characteristics of mafic (Phulad Ophiolite) and related rocks in the Delhi Supergroup, Rajasthan, India: implications for rifting in the Proterozoic. Precambrian Res. 48, 167–191.
Whitney, D.L., Evans, B.W., 2010. Abbreviations for names of rock forming minerals. Am. Mineral. 95, 185–187.
Wiedenbeck, M., Goswami, J.N., 1994. An ion-probe single zircon Pb age from the Mewar Gneiss at Jhamarkotra. Rajasthan. Geochim. Cosmochim. Acta 58, 2135–2141.
Wiedenbeck, M., Goswami, J.N., Roy, A.B., 1996. Stabilisation of the Aravalli craton of the north-western India at 2.5 Ga.: an ion-microprobe zircon study. Chem. Geol. 129, 325–340.
Williams, M.L., Jercinovic, M.J., Goncalves, P., Mahan, K., 2006. Format and philosophy for collecting, compiling, and reporting microprobe monazite ages. Chem. Geol. 225, 1–15.
Williams, M.L., Jercinovic, M.J., Hetherington, C.J., 2007. Microprobe monazite geochronology: understanding geologic processes by integrating composition and chronology. Ann. Rev. Earth Planet Sci. 35, 137–175.
Yadav, G.S., Pandey, U.K., Aravind, S.L., Panchal, P.K., Venkatesh, A.S., Sahoo, P.R., Chaturvedi, A.K., Rai, A.K., Parihar, P.S., 2016. U-Pb, Pb-Pb and Sm-Nd ages of Davidite within albitite zone from Bichun, Jaipur District, Rajasthan, India: Possible link between uranium mineralization and Grenvillian orogeny. Curr. Sci. 111, 907–913.